Algorithm Theoretical Basis Document (ATBD) Phase 2

glaciers cci

Prepared by:	Glaciers_cci consortium
Contract:	4000127593/19/I-NB
Name:	Glaciers_cci+D2.1_ATBD
Version:	2.1
Date:	31.08.2023

Contact:
Frank Paul
Department of Geography
University of Zurich
frank.paul@geo.uzh.ch

Technical Officer:
Anna Maria Trofaier
ESA Climate Office

Document status sheet

Iteration	Date	Changes	Approval
i1	09.03.2023	Initial draft	
i2	31.07.2023	Largest part of consortium Input included	
i3	31.08.2023	Missing parts added	F. Paul

The work described in this report was done under ESA contract 4000127593/19/I-NB, Contract Change Note 1. Responsibility for the contents resides with the authors who prepared it.

Author team:
Andreas Kääb, Désirée Treichler (GUIO), Thomas Nagler, Jan Wuite (ENVEO), Tazio Strozzi, Andreas Wiesmann (Gamma), Frank Paul, (GIUZ), Lin Gilbert (UCL).

Glaciers_cci Technical Officer at ESA:
Anna Maria Trofaier

Related documents

Acronym	Title	Document reference	Version	Date
[RD1]	Algorithm Development Plan	Glaciers_cci+_D2.4_ADP-Ph2	0.2	30.01.2023
[RD2]	Algorithm Theoretical Basis Document	Glaciers_cci+_D21_ATBD	1.0	10.10.2020

Table of Contents

1. Purpose

This document provides a detailed description of the development, testing and selection of the algorithms to generate the high-quality Fundamental Climate Data Records (FCDRs) data products required by the end-users as well as novel products made possible by exploiting new sensors and combinations. Building upon the achievements of the algorithm development in Glaciers_cci+ Phase 1, further algorithm improvements and possibilities for new algorithms were identified [RD1]. Here, the focus is on new or revised algorithms compared to the Glaciers_cci+ Phase 1 ATBD [RD2], i.e., this document is an extension of [RD2] and does not repeat algorithms covered in the earlier document, rather builds upon it.

This document is structured along the three identified focus areas, i.e., emerging possibilities from new sensors and data products, glacier facies mapping, and glacier surge detection. While the new topics glacier facies and surge detection have individual chapters focusing on specific new algorithms and associated novel products, the chapter on new sensors and data products is mainly structured along sensors/data products and their respective contribution to the Glaciers_cci+ product types, i.e., glacier area, elevation change and velocity.

According to the Statement of Work (SoW), the Glaciers_cci+ Phase 2 ATBD shall present (i) how sensors and data sets from the next generation of satellites may be used to monitor glaciers and improve and enhance observations of glacier change, (ii) new methods and products that support the understanding of glacier instabilities, specifically glacier surges and glacier facies, and (iii) extend existing time series of glacier variables further in time through historic data streams. Due to the large methodological differences in generating the products, the topics listed above are described differently for each product. However, all Chapters follow the same principal structure (section headings) to keep them comparable.

2. New sensors and products

2.1 Glacier mapping with Landsat 9

2.1.1 Introduction

Landsat 9 was launched on 27.9.2021, about 8 years after Landsat 8 (launched 11.2.2013). For continuity with Landsat 8, it was decided to use the same spectral bands as for Landsat 8 (Fig. 2.1) with one small difference, the quantization of the signal in all spectral bands was increased from 12 to 14 bit, i.e. from 4096 to 16384 discrete values. This means that the same spectral bands as for Landsat 8 can be used for glacier mapping with Landsat 9, but the threshold value to be applied for image segmentation might be different. The purpose of this test is to analyse the difference in the threshold values for two images acquired 8 days apart.

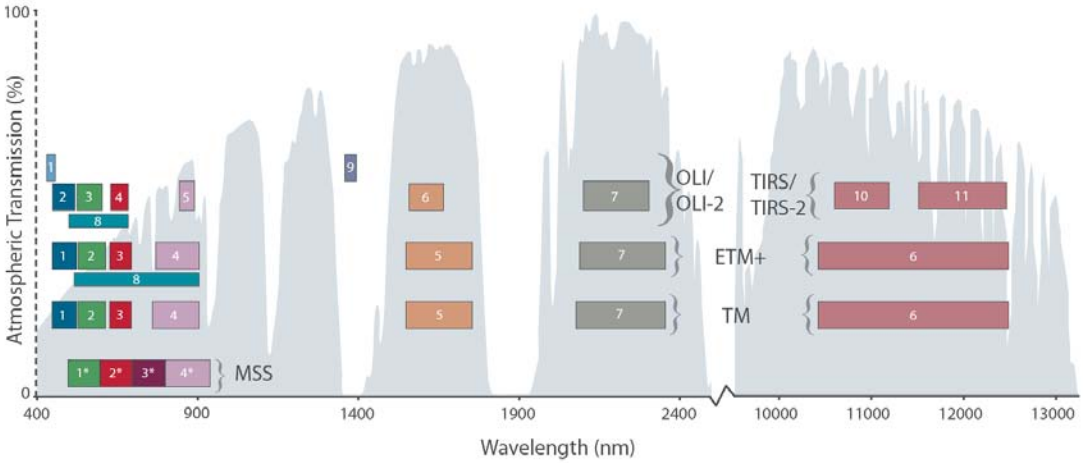

Fig. 2.1: Location of spectral bands for the four Landsat sensors MSS, TM, ETM+ and OLI/OLI-2. The grey-shaded region in the background is the atmospheric transmission. Taken from: https://landsat.gsfc.nasa.gov/satellites/landsat-9/landsat-9-bands/

2.1.2 Methods

The method used for glacier mapping (snow and clean to slightly dirty glacier ice only) is the band ratio method proposed by Paul (2002). It is based on a strong contrast enhancement when dividing the raw digital numbers (DNs) of a red or near-infrared band (where snow and glacier ice have high DNs) by the shortwave infrared (SWIR) band (where spectral reflectance and thus DNs of ice and snow are very low). This gives very bright glaciers and very dark other terrain in the ratio image. As the higher spatial resolution (15 m) panchromatic band can be used instead of the red band (cf. Paul et al. 2016), we resample the 30 m SWIR band to 15 m resolution using bilinear interpolation before the division. With a simple threshold a binary image or glacier map can be created from the ratio image. In pseudo-code, the algorithm reads:

```
IF (pan/SWIR) > th then 'glacier' else 'other'
```

with *th* the threshold to be applied, usually between 1.3 and 1.5 (for Landsat 8). The threshold is usually tested around these values in steps of 0.1 or 0.05 to find the best result, i.e. accurate

mapping of glacier ice in shadow. This is checked against the original image, usually a contrast enhanced version of a true colour composite image created from the red, green and blue bands (as RGB). As a note, the DNs of the SWIR band have to be converted to floating point format before the division. We compare the results from both sensors by overlaying the resulting vector outlines and calculating areas for selected individual glaciers or glacier complexes. The relative area differences are then compared to other uncertainties.

2.1.3 Processing line

The main steps of the processing line are:

1. select suitable images (no clouds over glaciers, end of ablation period)
2. download the required bands (for OLI/OLI-2: 2, 3, 4, 5, 6, 8)
3. resample the SWIR band 6 from 30 to 15 m using bilinear interpolation
4. divide the pan band by the SWIR band to create a ratio image
5. apply a series of thresholds to the ratio image and select the best one
6. possibly apply a filter to the binary image to remove noise (e.g. 3 by 3 majority)
7. set the value for other terrain to no data
8. convert the raster image to a vector file for further editing (e.g. adding debris cover)

For the tests performed here we skip step 6 and stop at step 8, i.e. further manual corrections are not applied to the resulting outlines.

2.2 Geometric consistency Landsat and Sentinel-2

2.2.1 Introduction

A recent study by Paul et al. (2023) for glaciers in New Zealand has shown that the geolocation of Sentinel-2 was different from Landsat 7 and a joint use of both sensors very difficult when it comes to smaller glaciers. This is also a well-known issue for Landsat 8 (Paul et al. 2016) and should have been corrected with the latest re-processing of all datasets. The geolocation shift by about 20-40 m is also an issue when combining glacier outlines derived from these sensors with independently geocoded datasets (e.g. ice divides derived from a DEM). Moreover, arbitrary shifts of about 20 m have also been detected for Sentinel-2 when combining datasets from different orbits and sensors (Sentinel-2A vs. 2B). Without a related co-registration, precise measurements of length changes or flow velocities are error prone. The purpose of this investigation is to analyse if the situation has improved for the latest version of the archived datasets.

2.2.2 Methods

We will use two methods to determine the geolocation consistency of current datasets: (M1) deriving glacier outlines (clean ice only) from band ratio mapping with subsequent overlay of resulting outlines and (M2) calculation of displacement vectors for stable terrain, similar to flow velocities. For both methods we will download test data from Landsat 7 / 8 and Sentinel-2 for the same region and from about the same acquisition date. These will then be processed with the two methods and possible shifts for glaciers and off glaciers calculated. Method M1 will be based on the Glaciers_cci standard processing method (band ratio with threshold) as described in [RD2] and the outline shifts or distortions will be analysed manually.

The second method M2 to determine orthoimage distortions and their effects on glacier mapping from repeat images will be based on the measurement of displacement vectors over sta-

ble ground between images from different orthoimage processing lines (here Landsat and Sentinel-2) following Kääb et al. (2016). If images are available from roughly the same time (±a few hours to days), the entire scene can be matched including glaciers as ice movement can then be neglected. The offset tracking between the images follows standard Glaciers_cci procedures as described in the former ATBD [RD2].

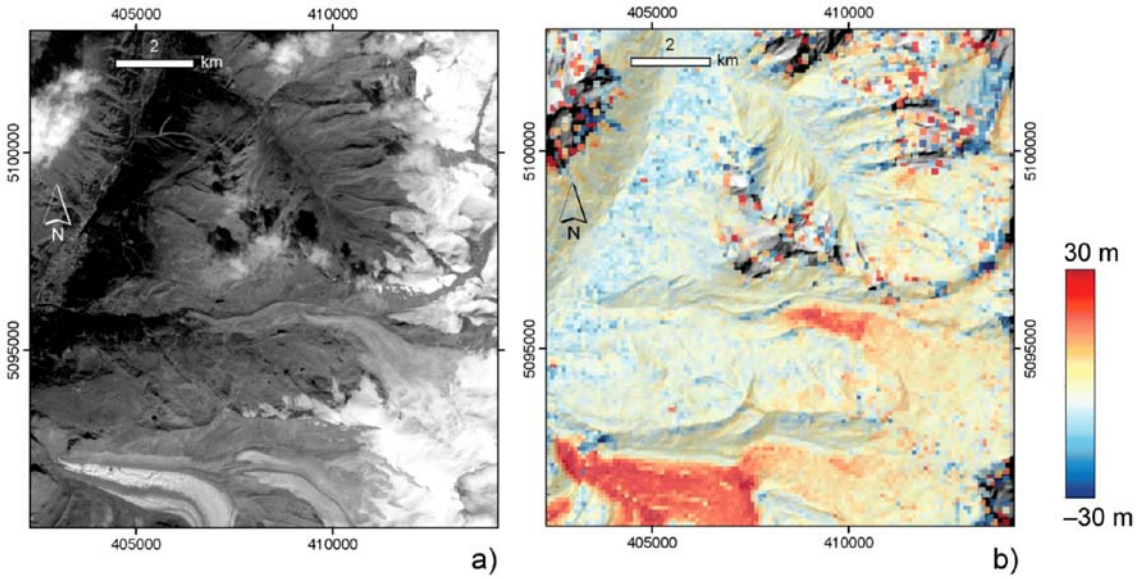

Figure 2.1: Cross-track offsets (b) between sections of a Landsat 8 and a Sentinel-2A (a) scene from 8 September 2015 (10:10 and 10:30 UTC, respectively) over Zermatt, Gorner Glacier and Findelen Glacier, Swiss Alps. Data voids in the offset field are due to mismatches over clouds. Colour-coded offsets underlain by a DEM hillshade. Distinct offsets over the glaciers are due to glacier thickness loss between the date of the DEM used for ortho-rectification and the image acquisition in 2015 (from Kääb et al. 2016).

2.2.3 Processing line

The processing line will consist of the following steps:
1. Selection of suitable scene and processing with the standard methods
2: Determination of shifts for glacier outlines (visually) and off-glaciers (automatic)
3. Statistical analysis and conclusions.

2.3 Glacier length changes from Keyhole images

2.3.1 Introduction

Determination of glacier length changes requires to have glacier outlines from two points in time and a centreline that crosses both lines so that a digital intersection of the two outlines with the centreline reveals the length change. For simplicity, we look at glaciers with a simple geometry of the tongue and the terminus. For the derived dataset we focus on usual glaciers. We focus on usual glaciers in the central Karakoram but also include some surge type glaciers for comparison. Glacier outlines from the GAMDAM2 dataset by Sakai (2019) are used as a starting point. These are then modified for changing terminus positions from different points in time starting with Keyhole images in 1961. How many further steps in time can be considered will depend on the observed changes. These should exceed two image pixels for a reliable determination of glacier fronts. Due to the geolocation differences described above (Section 2.2) we will only use Corona/Hexagon and Landsat images for this assessment.

2.3.2 Methods

As mentioned above, the length changes are determined from a simple digital intersection of glacier outlines with a centreline. This will transfer the ID of the glacier to the centreline so that glacier specific changes can be easily extracted. As we start with the GAMDAM2 glacier inventory that is also part of the Randolph Glacier Inventory (RGI) 7.0, we will use the centrelines created by the RGI team for RGI 7.0 as a starting point. Glacier outlines near the termini will be digitized manually using contrast enhanced true or false colour composites of the original satellite images in the background. It is planned to have such outlines for about every ten years, i.e. around 1960, 1970, 1980, ... 2020 so that about six values of change can be derived for the selected glaciers. Due to clouds, image coverage etc. the length change values to be obtained will vary for each glacier.

2.3.3 Processing line

As creation of the dataset is highly interactive, we here provide only a rough overview of the main steps:

1. selection of suitable satellite images (from Corona/Hexagon and Landsat)
2. point shape file indicating surge-type glaciers
3. selection of glaciers to be analyzed for the images available
4. download of glacier outlines and centrelines from RGI 7.0
5. digitizing of extents (terminal regions) for the selected glaciers and satellite images
6. intersection of centrelines with digitized extents
7. compilation of data per glacier (ID, coordinates, size, length t1, length t2, ...)
8. creation of plots for visualization

2.4 Sentinel-3

2.4.1 Introduction

Sentinel-3 radar altimetry data has been available since 2016 from Sentinel-3A and since 2018 from 3B. Unlike CryoSat-2, the Sentinels follow 27-day repeating orbits with maximum latitude at 81.35°N, leading to track separations that vary widely down the length of Greenland, from close spacing at the north to about 50 km in the far south. The orbits of the two satellites are offset so that the tracks from one are centred between the tracks from the other, bringing the track separation for the pair down to about 25 km in the south. Over the Greenland periphery this spacing is too large to observe many of the smaller southern glaciers, and the orbit does not reach the far north, but we will attempt to retrieve time-series of elevation changes wherever possible using an along-track processing method developed for ice sheet outlet glaciers (Maddalena, 2021).

Recently ESA has released pilot products from Sentinel-3 specifically dedicated to the land ice user community[1]. These 'thematic' products improve on the initial level 2 data releases, especially over difficult terrain. They include an extended radar echo window to retain the full radar echo, even over a fast-changing surface, and an improved slope model derived from the Helm et al. (2014) DEM. These will be used in the Greenland peripheral glaciers study, with each satellite processed separately and their results combined where possible. It may also be

[1]https://sentinels.copernicus.eu/web/sentinel/-/copernicus-sentinel-3-stm-land-thematic-products-operationa-release-of-pilot-data-set/1.6

possible to combine them with the results of the CryoSat-2 part of the Glaciers_CCI+ Phase 2 project, see Section 2.5 below.

2.4.2 Methods

The aim of the initial processing is to produce time-series with repeat-cycle temporal resolution at three different areal levels;

- regular along-track spacings
- geographical grid
- whole glacier

Initially, the along-track time-series will be made by migrating data points from each cycle to a set of central ground track locations using a slope model. These can then be gridded geographically and empty grid cells at each cycle for each glacier filled by interpolation by universal kriging, guided by a DEM to take into account local hypsometry. A similar interpolation will be performed for CryoSat-2 data (see Section 2.5), but Sentinel-3 data is likely to be much sparser. Finally, all grid cells per cycle within each glacier outline will be averaged to produce a whole-glacier time-series.

Surface elevation change rate along the time-series at all of these areal levels will be modelled by simple linear regression, both for the full mission so far, and in a moving 5-year window, stepping at one year. As the uncertainties in this dataset are much larger than the correction for Glacial Isostatic Adjustment (GIA), GIA will not be included in the processing.

2.4.3 Processing line

Input data comes from the Sentinel 3 LAND thematic product[2]. This is a level-2 product, providing location and surface elevation corrected for ground slope effects and corrected for geophysical effects, i.e. dry tropospheric, wet tropospheric, ionospheric, solid earth tide, pole tide and ocean loading tide. Two retrackers are provided - Offset Centre of Gravity (OCOG) and Ice Sheet, but the former is selected as preliminary studies show that more data are generated by this retracker. A filtering step will remove data points whose elevations differ by more than 100 m from the Arctic DEM.

Data on uncertainty comes from the Sentinel 3 Surface Topography Mission Annual Report for 2021[3], which reports a calibration exercise against Operation IceBridge over north-west Greenland, giving a table of accuracy against surface slope. Auxiliary data comes from the RGI glacier outlines[4] and the Arctic DEM[5] at 500 m resolution.

For each glacier, nadir ground tracks containing data are identified. These will not repeat exactly due to orbital perturbations, so an ‘averaged’ track is derived by linear fit to the nadir tracks on a north polar stereoscopic projection. This approximation is reasonable for the short tracks crossing the peripheral glaciers. Reference points 300 m apart are defined along the averaged track. Each reference point is the centre of an area bin that is 300 m along-track and 10 km across-track (the maximum extent likely for echo returns from highly sloping terrain). A

[2]https://sentinel.esa.int/web/sentinel/technical-guides/sentinel-3-altimetry/products-and-algorithms/baseline-collection-005-processing-status
[3] https://sentinels.copernicus.eu/fr/web/sentinel/technical-guides/sentinel-3-altimetry/mission-performance
[4] https://www.glims.org/RGI/
[5] https://www.pgc.umn.edu/data/arcticdem/

time-series is assembled at each reference point, containing one data point per orbital cycle, where possible. For Sentinel-3, that is a temporal resolution of 27 days. Figure 2.2 shows all Sentinel-3A data from 28 cycles over an ice cap with an area of approximately 500 km^2, and the layout of the area bins for an example set of tracks.

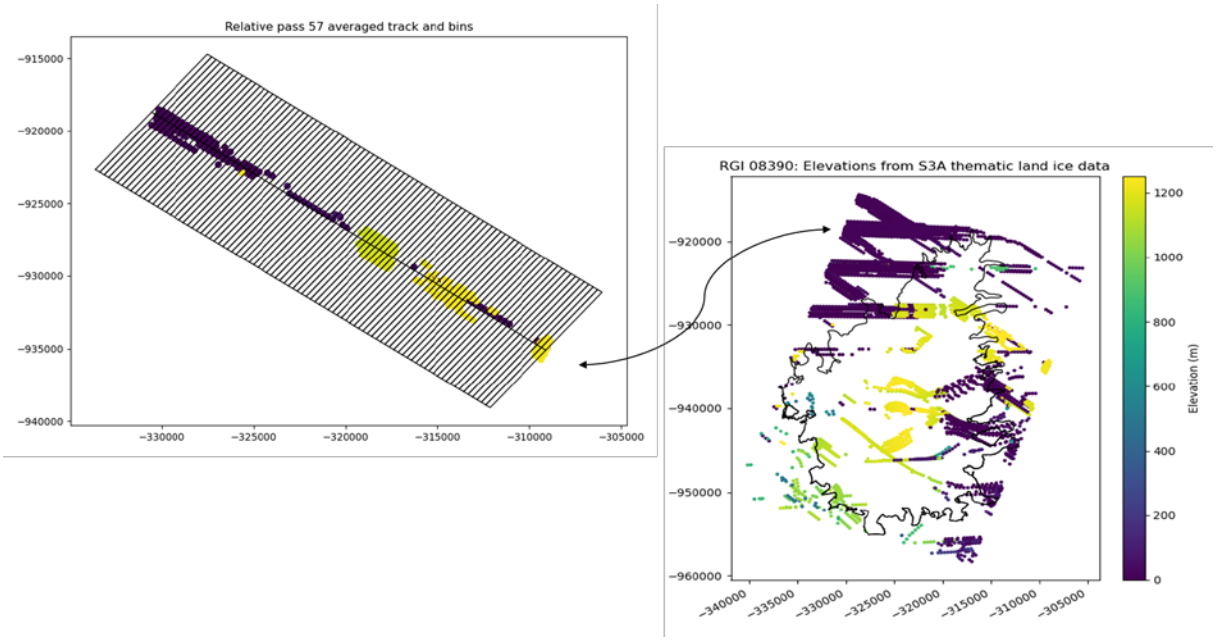

Figure 2.2: Repeat track binning example. Left: data for 28 repeats of relative pass 57, with averaged track along centre and area bins as rectangles perpendicular to track. Right: elevations from 28 cycles, showing data distribution over example ice cap RGI 08390, with an area of about 500 km^2.

In practice, only one or two data points per cycle will be found within each area bin. The actual data locations are not at nadir, but at Point of Closest Approach (POCA) where the radar wavefront first encounters the surface. The data point closest to the reference point is selected, and migrated to the reference point, i.e. its elevation is altered to account for the slope between itself and the reference point. This is done by finding the elevation difference between the two points on the Arctic DEM and adding the difference to the data point elevation. Uncertainties at the data point level come from the accuracy vs. slope table for the Sentinel-3 data point, and the DEM accuracy at both locations, summed in quadrature.

Once the reference point time-series are complete, they can be averaged within a geographical grid. The grid chosen uses a 500 m by 500 m polar stereographic projection, to match the CryoSat-2 swath point product processing grid, as described in Section 2.5. The per-cycle grids will contain many empty cells due to the Sentinel-3 orbits, but if at least 10 cells are present in a given cycle then empty cells will be filled by universal kriging guided by the Arctic DEM, again as for the CryoSat-2 processing. Uncertainties come from either the standard deviation of the input data in each cell, or the estimates for the interpolated cells provided as part of the Kriging algorithm. Finally, the interpolated grids will be averaged within the glacier outline to produce a single glacier-wide time-series. Uncertainty will come from the standard deviation of the inputs.

Elevation change rates at each areal level are derived by linear fitting to the elevation time-series, over both the full mission period and for a 5-year wide window, moving in 1-year

steps. At minimum 5 monthly-averaged data points spanning at least 3 years must be present within the time period under consideration before a fit is performed.

The output product will consist of the time-series and elevation change rate estimates at each areal level. Figure 2.3 shows the processing line for surface elevation change from a single Sentinel-3 (A or B) thematic land ice product.

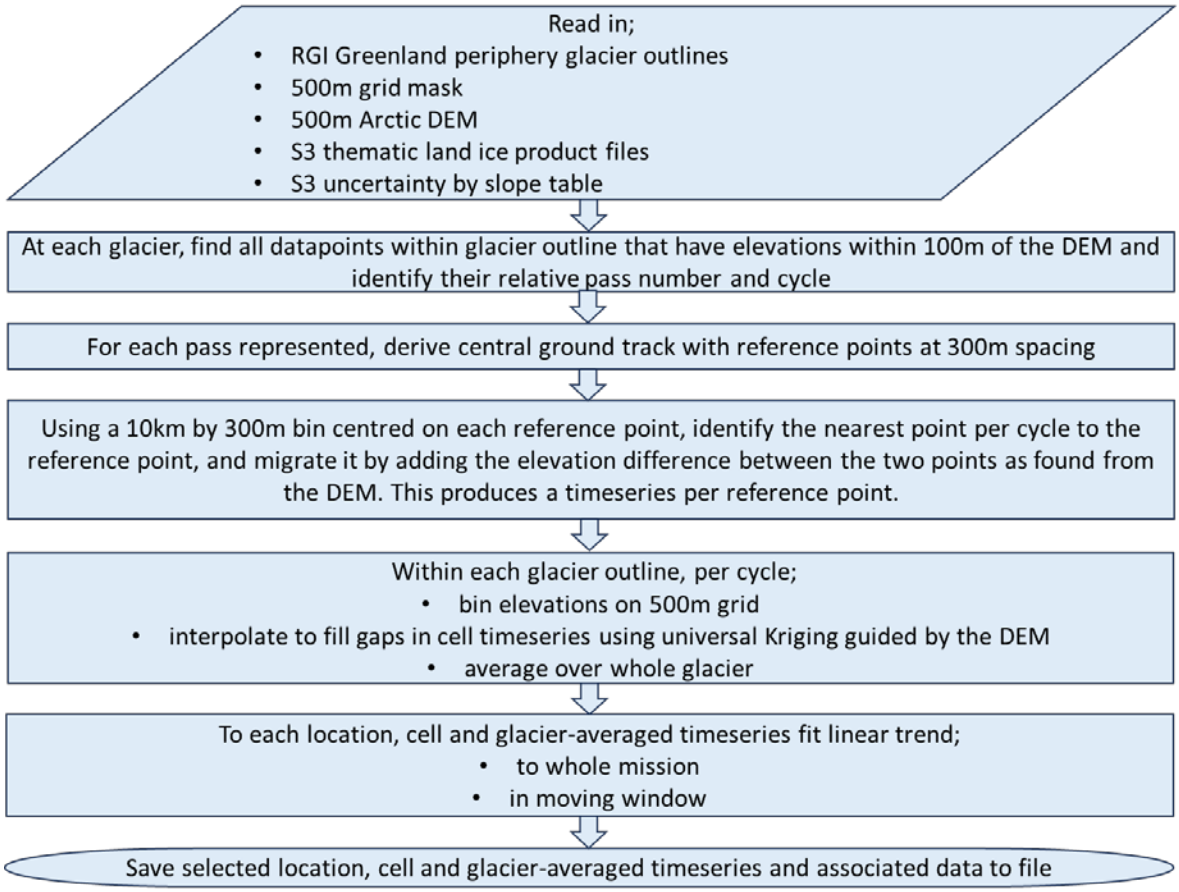

Figure 2.3: Processing line - surface elevation change from thematic land ice product (to be applied to Sentinel-3 A and B separately).

2.5 Cryosat-2 swath mode

2.5.1 Introduction

Cryosat-2 radar altimetry data has been used to determine trends in surface elevation changes over ice sheets for many years, retrieving only one surface elevation from each radar echo, known as the Point Of Closest Approach (POCA). For example, Shepherd et al. (2019) uses this method to generate a long-term mass balance time-series for the Antarctic ice sheet.

More recently, the swath processing technique has been used to extract information from the full echo waveform, allowing elevation retrieval along a surface swath, which increases spatial and temporal coverage dramatically. Atypical waveforms, which do not have a recognisable POCA, may yield data using this method. Swath processing is possible where echoes have good coherence and amplitude, and surface slopes are up to a few degrees. The waveform is

'unwrapped' with reference to a DEM, mapping the range, across-track look angle, platform attitude and orbit parameters of each echo into a swath comprised of multiple elevation points above a reference ellipsoid. For example, Foresta et al. (2016) maps the six major Icelandic ice caps at 500 m resolution using this technique.

In 2022, the CryoTEMPO-EOLIS swath products were made publicly available[6]. Both a point product, containing all the retrieved swath data points, and a gridded product at 2 km resolution derived from the point product, are provided. Both products cover the full Cryo-Sat-2 mission period, and the full extent of the Greenland peripheral glaciers and ice caps. In the gridded case, the 'Greenland' area is used, in the point case, 'Greenperi' is used.

We will use both products to assess their performance over the Greenland periphery, where rugged terrain is always difficult for radar altimetry. Both products will be used to produce gridded time-series, and surface elevation change will be modelled from them. The gridded product only needs to be stacked and filtered by RGI outline. The point product will be processed in a similar way to other glacier swath mode studies, such as Tepes et al. (2021) and Jakob and Gourmelen (2023). This method uses much of the same processing flow as the Glaciers_CCI+ Phase 1 altimetry over the Russian Arctic see [RD2], but with higher resolution, a simpler surface model, and an added interpolation step using universal Kriging guided by a DEM. If possible, Sentinel-3 data (see Section 2.4 above) will be merged with the CryoSat-2 data to produce joint time-series, to further increase data density.

2.5.2 Methods

The aim of the processing is to create gridded time-series of elevation change and derive elevation change rates from them. In both cases the first step is defining the grid cells of interest, as the peripheral glaciers cover only a small, but widespread, area of Greenland. Only glaciers which are weakly connected or unconnected to the ice sheet are of interest. The RGI outlines are used to calculate the glacierized proportion of each cell, and those over 50% glacierized are selected, regardless of grid resolution.

The gridded swath product is a set of monthly DEMs, which will be stacked to provide time-series per grid cell. The cells are large, at 2 km by 2 km resolution. Surface elevation change rate is modelled by simple linear regression, both for the full mission so far, and in a moving 5-year window, stepping at 1 year. As the uncertainties in this dataset are much larger than the correction for Glacial Isostatic Adjustment (GIA), GIA will not be included in the processing.

The point swath product is treated similarly to the single-mission processing in [RD2]. This time the grid is 500 m by 500 m, which has been successfully used in glacierized regions. In each cell, data points from the full mission within the glacier outlines are assembled and a surface model is fitted to the data. From this model, residual elevation anomalies can be derived, and the mean anomaly per cell calculated at regular one-month intervals. Within each individual glacier outline, at each time-stamp, universal kriging, guided by a DEM, will be used to gap-fill cells with no recorded data. A glacier-wide time-series will be made by averaging the filled dataset. At both cell and glacier level, the change rate is modelled as for the gridded swath product, using simple linear regression for the full mission and a moving window. Again, given the size of the uncertainties, GIA correction will not be applied. Figure 2.4

[6] https://cryotempo-eolis.org/

shows an example of the guided kriging for one month of gridded data, over RGI 08390, the same example ice cap as in section 2.4, above.

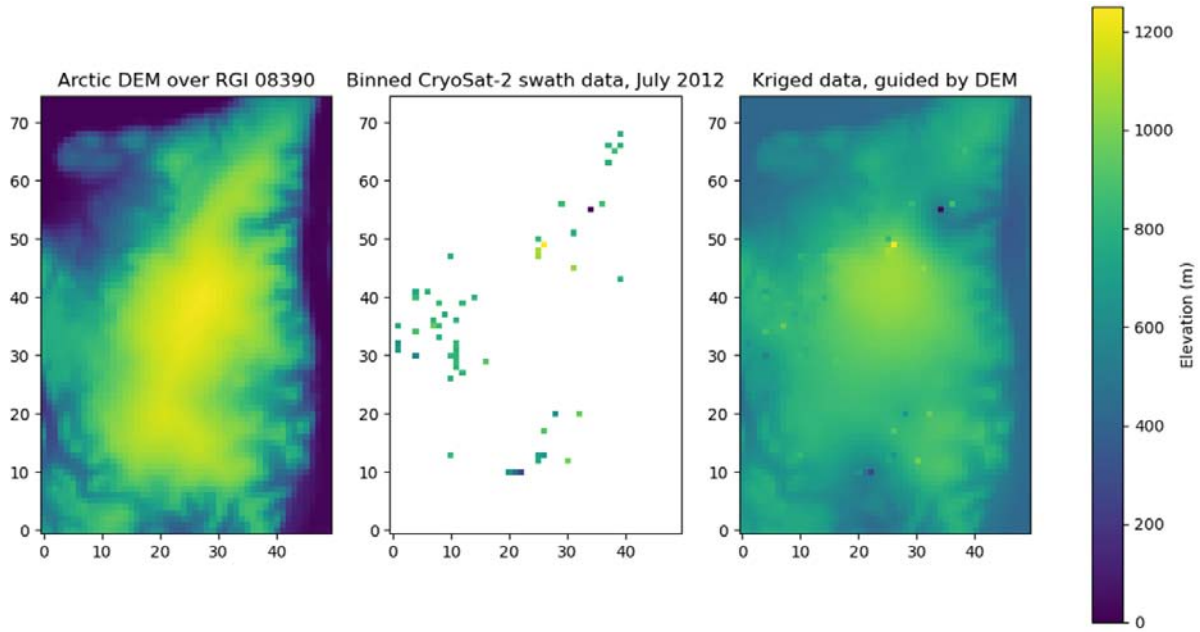

Figure 2.4: Left to right: DEM, gridded data for July 2012, data kriged by DEM.

If there is sufficient data to cross-calibrate the point swath product with Sentinel-3 time-series, then the same method will be used as in [RD2], where multiple regression is applied to calculate the bias between each pair of time-series. The change rate will then be derived from the combined time-series, as for the single time-series above.

2.5.3 Processing line

Input data comes from the CryoTEMPO-EOLIS baseline 1 products, as baseline 2 is not yet available for the full CryoSat-2 mission timespan. These products are derived from CryoSat-2's baseline D retracked echo waveforms, which give location and surface elevation corrected for ground slope effects and corrected for geophysical effects, i.e. dry tropospheric, wet tropospheric, ionospheric, solid earth tide, pole tide and ocean loading tide. Data are filtered by backscatter power and coherence to remove weak signals, and by comparison to a reference DEM for both individual points and the median absolute deviation of the swath. Each data point is given an uncertainty based on the binned combination of backscatter power and coherence, distance to POCA, slope and surface roughness, calibrated against the ICESat-2 ATL06 dataset. Auxiliary input data comes from the RGI glacier outlines[7] and the Arctic DEM[8] at 500m resolution.

Preliminary processing establishes the grid and mask used to locate grid cells of interest. This is followed by two separate processes, one using the gridded swath product as input and one using the point swath product. A final cross-calibration between the point product and Sentinel-3 time-series, where possible, will yield a joint time-series product.

2.5.3.1 Grids and masks

[7] https://www.glims.org/RGI/
[8] https://www.pgc.umn.edu/data/arcticdem/

Grids are defined to align with the CryoTEMPO-EOLIS 2 km resolution grid, which uses the northern polar stereographic projection EPSG 3413.

Gridded swath processing mask: To locate the cells of interest, a 200 m resolution sub-grid is calculated, and cells whose centres are within the outlines of the glaciers of interest (i.e. those weakly connected or unconnected to the ice sheet) are masked. If a majority of the sub-cells within a given 2 km resolution cell are masked, then the 2 km cell is also masked.

Point swath processing mask: This uses a 500 m resolution grid. If a cell contains any point product data within the glacier outlines, then that cell is masked and used.
Figure 2.5 shows the processing line for gridding and masking.

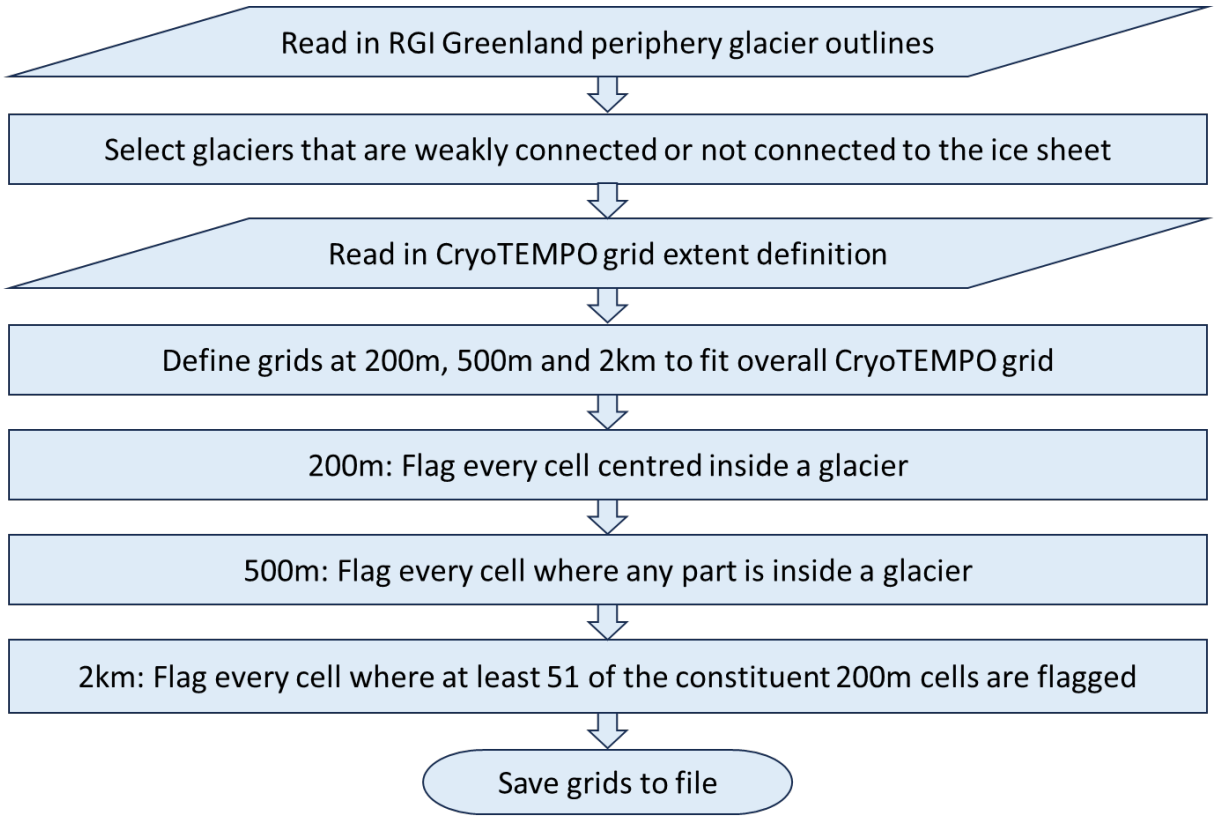

Figure 2.5: Preliminary processing line - grids and masks.

2.5.3.2 Gridded swath product

The Greenland products are read in, and cells selected according to the 2 km mask. The full grid structure is not retained, as it would consist mainly of empty cells. Instead, cell indices and centre locations for each masked cell are associated with a time-series for that cell. Monthly input products are stacked to produce the time-series. Each input data point comes with an associated uncertainty, which for this product and baseline is constant across all cells and months. Time-series containing at least 5 data points, which span a period of at least 3 years, are selected. This is a minimal filtering set, to retain as much data as possible.

Elevation change rates are derived by linear fitting to the elevation time-series over the full mission period. Rates are also found for a 5-year wide window, moving in 1-year steps, as long as the minimal filtering conditions are present within the window.

Uncertainty sources come from the input data as given and the modelled fit. The total uncertainty on the surface elevation change rate is the RMS of the input uncertainties divided by the timespan involved, summed in quadrature with the standard deviation of the linear fit.

The output product will consist of the gridded time-series and derived change rates. Figure 2.6 shows the processing line for surface elevation change from the gridded swath product.

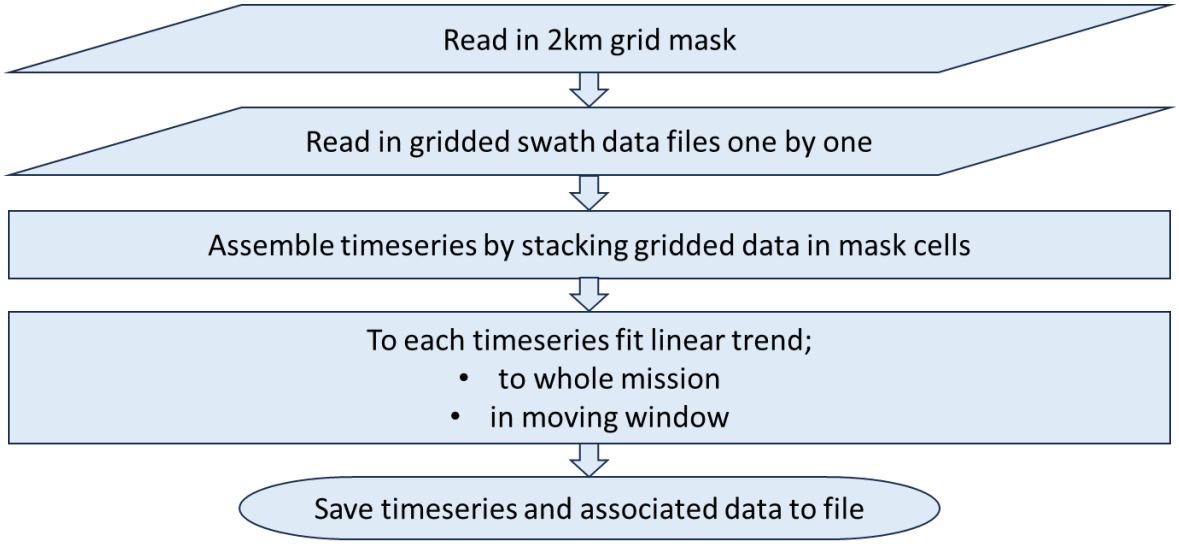

Figure 2.6: Processing line - surface elevation change from gridded swath product.

2.5.3.3 Point swath product

The 'Greenperi' area products are read in, and cells selected according to the 500 m mask. As for the gridded product, the full grid structure is not retained as it would consist mainly of empty cells. Data is binned by cell. As a first filtering step, cells containing at least 100 data points, which span a period of at least 5 years, are selected.

For each cell, a surface model is fitted, using the equation:

$$h\,(x,y,t) \;=\; a0 \;+\; a1\,x \;+\; a2\,y \;+\; (dh/dt)\,t$$

where h is height, x and y give location in polar stereographic projection, t is time and a0, a1 and a2 are constants.

The model fit uses a multiple regression, weighted by the uncertainties on each input data point. The differences between modelled and measured points are taken and their standard deviation found. Any points with a difference larger than 3 standard deviations are removed, and the fit iterated until either there are no outlying points left, or the cell no longer satisfies the filtering requirements above and is rejected.

The modelled surface is removed from the initial data points to provide the height anomaly dh due to changes over time, and this anomaly is averaged within a set of monthly time limits to produce a monthly time-series. The uncertainty at each timestamp is the RMS of the input data point uncertainties.

Elevation change rates are derived by linear fitting to the height anomaly time-series, over both the full mission period and for a 5-year wide window, moving in 1-year steps. Similarly to the gridded product, at least 5 monthly-averaged data points spanning at least 3 years must be present within the time period under consideration.

Uncertainty sources come from the uncertainties calculated for the height anomaly time-series and the modelled fit. The total uncertainty on the surface elevation change rate is the RMS of the height anomaly uncertainties divided by the timespan involved, summed in quadrature with the standard deviation of the linear fit.

A gridded output product will consist of these time-series and derived change rates. The grid cell time-series will also be used to produce a single time-series per glacier where possible. If at least 10 height anomaly data points are available within a glacier outline at a given month, then we attempt to fill the missing cells by universal kriging, with a spherical variogram model, guided by the Arctic DEM to take account of local hypsometry. Uncertainty estimates for the interpolated data points are provided as part of the kriging algorithm.

Elevation change rates can then be found for each glacier as a whole using the same linear fitting and constraints as for the individual grid cells, and calculating uncertainty in the same way. Again, the glacier output product will contain these time-series and derived change rates. Figure 2.7 shows the processing line for surface elevation change from the point swath product.

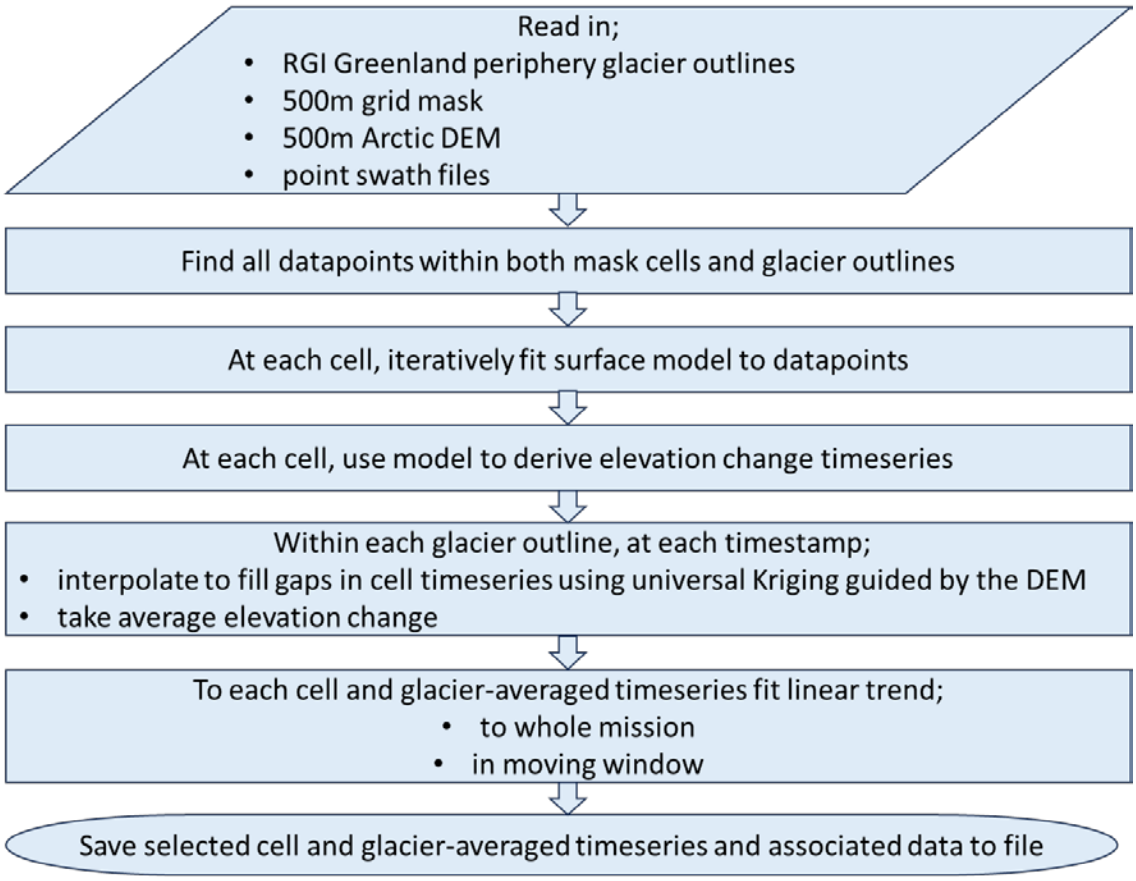

Figure 2.7: Processing line - surface elevation change from point swath product.

2.5.3.4 Joint product

Output products from the Sentinel-3 processing and the CryoSat-2 point swath product are read in, and cells containing time-series from both products identified. In each cell, the pair of time-series is cross-calibrated using a multiple regression method, assuming that the time-series as a whole takes a cubic polynomial form. This is the same method as used in [RD2] for multi-mission cross-calibration, but restricted to two missions. The independent variables for the regression are time, time squared, time cubed and a flag array to indicate the Sentinel-3 data points. The regression algorithm calculates a coefficient for each independent variable, and the coefficient for the mission flag array is the bias value needed to best adjust the Sentinel-3 time-series in line with CryoSat-2. This bias value is applied to every Sentinel-3 data point and the algorithm returns its standard deviation.

Once a combined time-series is achieved, elevation rates for the full CryoSat-2 mission period and the moving window can be calculated with linear fitting as above. In this case an extra term is necessary to account for the cross-calibration uncertainty. To convert to a rate uncertainty, the standard deviation of the bias is divided by the timespan involved, and summed in quadrature with the RMS of the height anomaly uncertainties divided by the timespan involved and the standard deviation of the linear fit, as above.

The combined time-series will also be used to produce a single time-series per glacier where possible, using the same kriging method as for the point swath product above. Again, elevation change rates will be calculated per glacier. Output products will be the time-series and derived change rates, both for the grid cells and the whole-glacier outlines. Figure 2.8 shows the processing line for surface elevation change from the joint product.

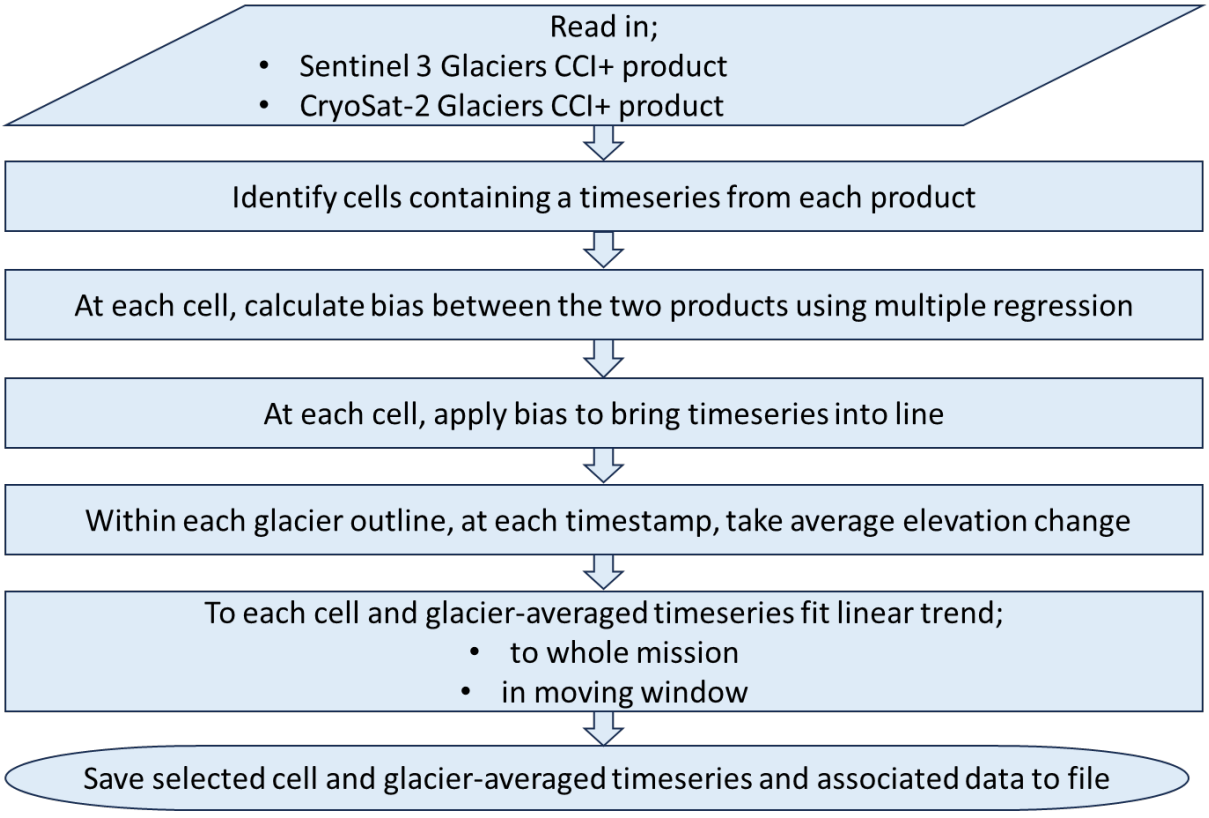

Figure 2.8: Processing line - surface elevation change from joint product.

2.6 ICESat-2

2.6.1 Introduction

ICESat-2's on-board laser altimeter provides a high resolution (100 m) DEM of Greenland in product ATL14, and a set of 3-monthly height change maps at up to 1 km resolution, and their associated elevation change rates, in product ATL15. At the time of writing, the ATL15 product covers dates from March 2019 to March 2022. Figure 2.9 shows the metadata summary plot of mean elevation change rates for the full period. As can be seen, the dataset does not fully cover the peripheral glaciers, especially in the far north. For full description see Smith et al. (2022).

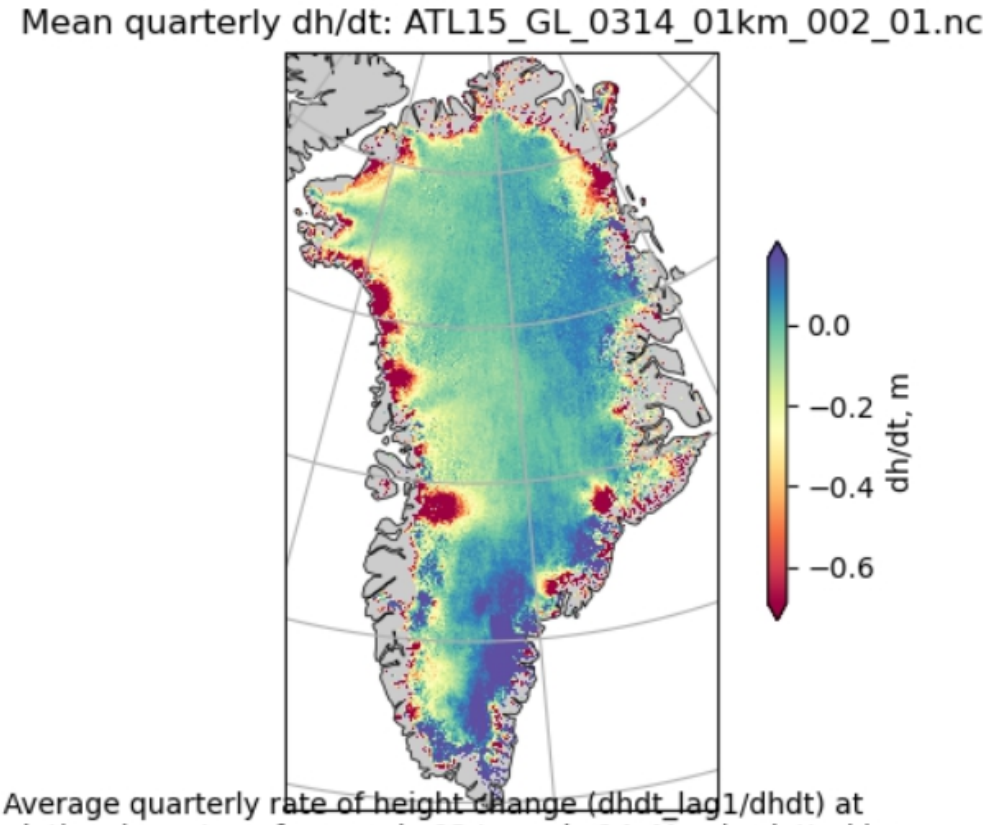

Figure 2.9: ICESat-2 ATL15 mean elevation change rates 2019-2022 from product metadata.

2.6.2 Methods

The aim of the processing is to create a specific subset of the ICESat-2 products over the Greenland peripheral glaciers that are weakly-connected or unconnected to the ice sheet, combining elevation time-series and elevation change rates, similar to those produced for Sentinel-3 and CryoSat-2 (Sections 2.4 and 2.5, above).

The ATL15 product is already gridded using the same north polar stereographic projection as is used in the Glaciers_CCI+ products for Sentinel-3 and CryoSat-2 in Sections 2.4 and 2.5 above. The highest resolution available is 1 km, so each grid cell will be used for comparison

to four of the Glaciers_CCI+ product grid cells - the cell edges coincide exactly, so there is no need for re-binning.
The time-series within the ATL15 product are provided as the change to the DEM elevation given by the ATL14 product, spanning 3.5 years in total. The two products will be summed to provide an elevation time-series. The derived change rates for periods from 3 months to 3 years are also provided in ATL15. These measurements will also be averaged glacier-wide.

2.6.3 Processing line

Input data comes from the current ICESat-2 ATL14[9] and ATL15[10] products, version 2, for the Greenland area, accessed in July 2023. Since the height anomaly time-series and elevation change rates are already provided in ATL15, there is no need for further processing of these measurements. The highest resolution (1 km) grids will be selected.

Elevation time-series will be assembled by adding the height anomaly time-series from ATL15 to the DEM from ATL14. Since these time-series are supplied at different grid resolutions, the DEM (at 100 m resolution) will be averaged over each cell of the height anomaly time-series before addition. In each cell, the uncertainty of the DEM elevation will be taken as the RMS uncertainty of the input elevations and added in quadrature to the uncertainty of each individual height anomaly.

Elevation and elevation change time-series at each 3-month timestamp will be averaged within each glacier outline to produce a single glacier-wide time-series, if necessary using universal kriging as in the point swath data product above. Output products will be the time-series and derived change rates, both for the grid cells and the whole-glacier outlines. Figure 2.10 shows the processing line for surface elevation change from ICESat-2 products.

[9] https://nsidc.org/data/atl14/versions/2
[10] https://nsidc.org/data/atl15/versions/2

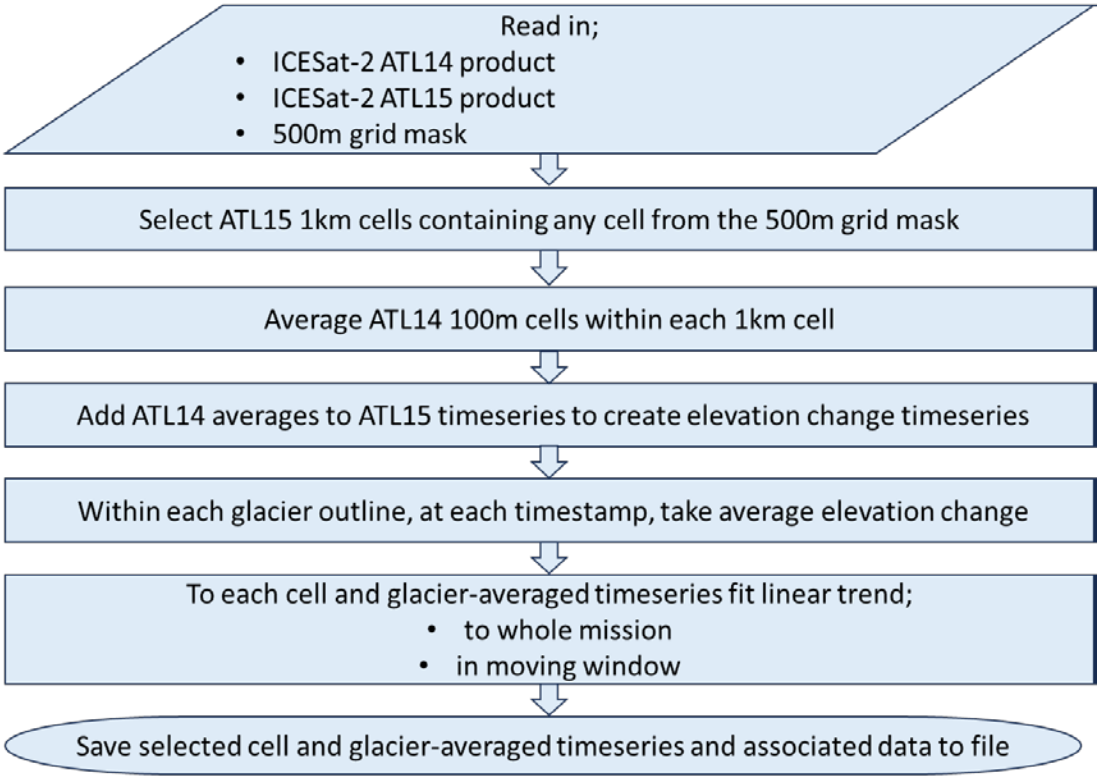

Figure 2.10: Processing line - surface elevation change from ICESat-2 products

2.7 SAOCOM A/B

2.7.1 Introduction

The SAOCOM-1 SAR mission is composed of two satellites (SAOCOM-1A and 1B) with L-band polarimetric SAR launched in 2018 and 2020 respectively. The mission is managed and operated by the Comisión Nacional de Actividades Espaciales (CONAE) of Argentina. SAOCOM has a revisit time of 16 days with one satellite and 8 days with the constellation. There are two main operational modes, Stripmap (SM) and TopSAR, operating with nine beam modes (S1-S9) with incident angles ranging from 20 to 50 degrees (Figure 2.11, Figure 2.12). SAOCOM provides L-Band SAR data over glaciers and ice caps with 8 and 16 days repeat cycle as a background mission, meaning without systematic acquisition plan.

The use of SAOCOM SAR for ice velocity (IV) retrieval and the synergistic use of L-Band and C-Band SAR data as provided by SAOCOM and Sentinel-1 is expected to improve monitoring of ice dynamics. Compared to C band (e.g. Sentinel-1), L-Band provides improved signal correlation especially in areas with changing surface conditions. By using L-Band SAR, the use of the InSAR method can be extended to cover also faster moving areas than possible with C-band as these data have a reduced fringe frequency in shear zones and fast-moving areas enabling more reliable phase unwrapping. On the other hand, L-Band is more sensitive to disturbances by ionospheric effects than shorter wavelengths.

For first algorithm development and evaluation we selected test data covering the Southern Patagonian Icecap (SPI), further test areas will be selected during the project. Data access to the SAOCOM L1A (SLC) SM archive was secured through a data request proposal. For InSAR we considered data acquired with 8-day repeat cycle. Offset-tracking was tested for mul-

tiple repeat cycles. In total 40 SLC images were processed covering the period June-October 2022 (Figure 2.13).

Type	Synthetic Aperture Radar (SAR)
Center Frequency	1275 MHz (L-band)
Maximum Bandwidth	50 MHz
Transmit Peak Power	6.7 kW
Operational Modes	StripMap TopSAR
Swath Width	13 - 67 km (beam dependent) for StripMap 109 - 389 km (beam dependent) for TopSAR
Polarization Modes	Single, dual or quad polarization (technological Compact Polarization modes also available)
NESZ (Noise Equivalent Sigma Zero)	< -34 dB for StripMap and TopSAR quad polarization modes < -28dB for StripMap and TopSAR dual and single polarization modes
Antenna Looking Angle	left or right side of path (right side is default)
Incidence Angles	18-50°
Data Quantization	4 bit Block Adaptive Quantization
Duty Cycle	15% (about 15 minutes per orbit, depending on selected datatakes modes datarate and available ground stations)

Figure 2.11: Overview of SAOCOM SAR mission characteristics (source: https://earth.esa.int/)

Acquisition Mode	Polarization Mode	Swath Width	Spatial Resolution	Incidence Angle Range (min)
Stripmap	Single (SP), dual (DP) or quad (QQ)	SP & DP: 30 km - 67 km QP: 13 km - 30 km	QP: 10 m el x 6 m az (L1A SLC) DP & SP: 10m el x 5 m az (L1A SLC)	SP & DP: 21° - 50° QP: 18° - 35°
TopSAR narrow	Single (SP), dual (DP) or quad (QQ)	TNA QP >109 km TNB QP >108 km TNA DP & SP >174 km TNB DP & SP >150 km	QP: 10 m el x 50 m az (L1A SLC) DP & SP: 10 m el x 30 m az (L1A SLC)	TNA QP: 18°- 27° TNB QP: 27°- 35° TNA DP & SP: 25°- 38 TNB DP & SP: 38°- 47°
TopSAR wide	Single (SP), dual (DP), quad (QP), or compact (CP)	TW QP >217 km TW DP & SP & CP >352 km	QP: 10m el x 100m az (L1A SLC) DP & SP: 10m el x 50 m az (L1A SLC)	TW QP: 18°- 35° TW DP & SP: 25°- 48°

Figure 2.12: Overview of SAOCOM acquisition modes and specifications (source: https://earth.esa.int/)

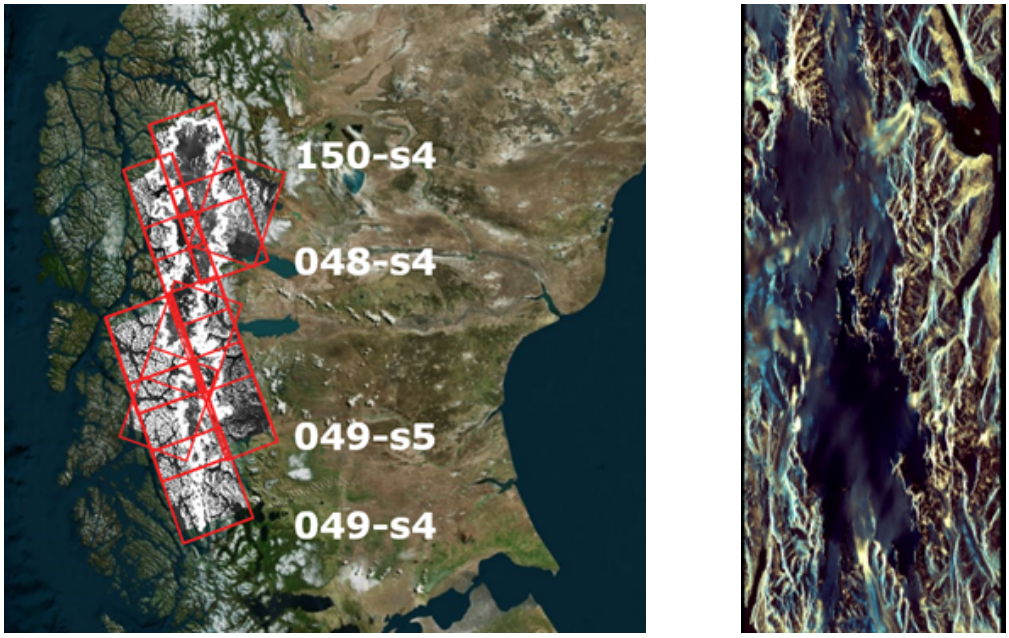

Figure 2.13: Left) SAOCOM coverage of the Southern Patagonian Icecap, indicating path and beam mode. Right) Example SLC image (path 48, row, 366).

2.7.2 Methods

Available IV retrieval algorithms from Glaciers_cci+ Phase 1 [RD2] based on SAR interferometry (InSAR) and offset-tracking are adapted to SAOCOM data for ice surface velocity estimation of alpine type glaciers and ice caps. The product quality will be assessed by intercomparison with ice velocity products from contemporaneously acquired Sentinel-1 data or other available products, considering the suitability for different glacier types (small glaciers to ice caps). Evaluation of the test results is on-going.

2.7.3 Processing line

The InSAR processing line is depicted in Fig. 4.2 of [RD2]. Adaptation of this processing line for SAOCOM data focus on handling large baselines and automatization of co-registering. SAOCOM data, by combining orbital data, a DEM and refinement using local matching, which is needed due to the reduced quality of the orbital state vectors. For this refinement we use a long-term averaged ice velocity map derived from Sentinel-1 offset tracking. The focus is also on improvements for correction of ionospheric artefacts, which can be of particular importance for use of L-band SAR data, but did not affect our current study area in Patagonia.

By using L-Band SAR the use of the InSAR method can be extended to cover faster moving areas than possible with C-band, as these data have a reduced fringe frequency in shear zones and fast-moving areas enabling more reliable phase unwrapping. The interferometric processing consists of co-registration SLC images, generating an interferogram and subtracting the flat earth and topographic phase contributions (Figure 2.14). The processing yields wrapped displacement interferograms, which is then unwrapped, the unwrapped phase is calibrated against stationary ground control points and subsequently converted into line-of-sight (LOS) velocity. If no fixed ground control points are available over the area of interest, the unwrapped phase is calibrated against a velocity template (e.g. multiannual ice velocity map from Sentinel-1 offset-tracking) using only slow-moving ground control points. The resulting LOS velocity maps are used for inversion to retrieve a 2-D surface velocity field.

Provided that velocity measurements from at least two different viewing geometries (i.e. ascending and descending tracks) are available for a given point, the easting (v_x) and northing (v_y) velocity components can be determined. When LOS velocity is only available from one view direction, the velocity components can be derived from combining the flow direction derived from OT with the InSAR line-of-sight velocity measurements, assuming stability of the flow lines over time. The principle of the method is further detailed in [RD2]. Using SAOCOM data we investigate this method for combining L- and C-Band interferometric data for ice velocity monitoring using InSAR.

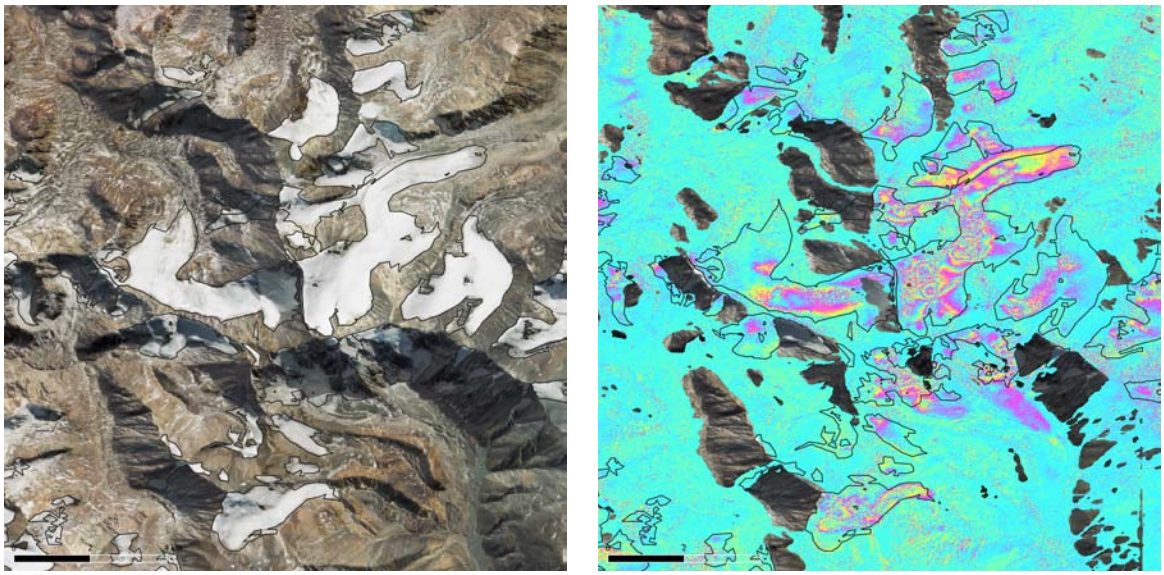

Figure 2.14: SAOCOM 8-day differential interferogram from 2022.08.25 to 2022.09.02 with Bperp of -3 m over part of the Central Andes (Argentina). Ice divides (black) are from RGI 5.0. The optical image to the left is shown for comparison.

The offset-tracking processing line is depicted in Fig. 4.11 of [RD2]. The generalised processing line for offset-tracking could be adapted to SAOCOM data. Figure 2.145 (left) shows the ice velocity of Viedma Glacier derived using offset tracking from a single 8-day repeat SAOCOM image pair. The L-Band provides excellent coverage and compares well with the long-term averaged Sentinel-1 derived ice velocity (Figure 2.145; right).

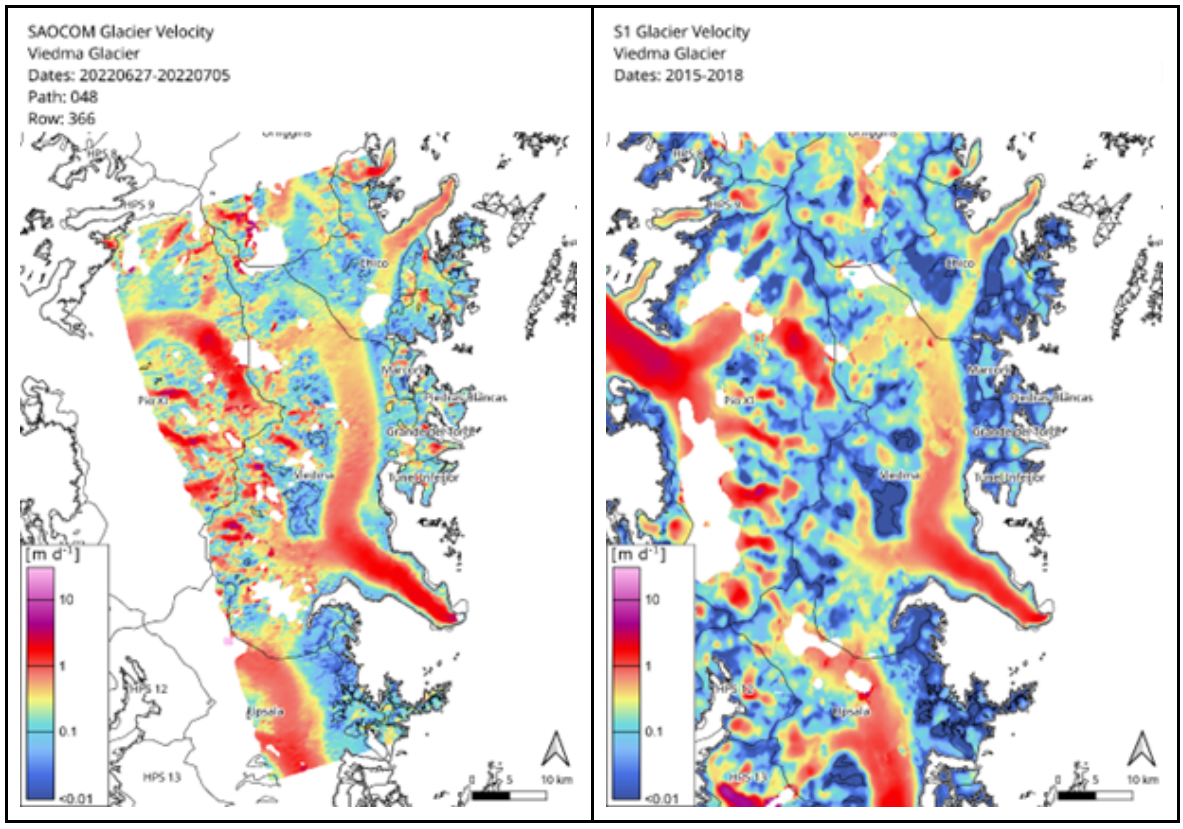

Figure 2.15: Left) Glacier velocity of Viedma Glacier derived from offset tracking using a SAOCOM image pair acquired on 27 June 2022 and 5 July 2022. Right) Long-term averaged velocity of the same area from offset tracking using Sentinel-1 data acquired between 2015 and 2018.

2.8 ICEYE

2.8.1 Introduction

The ICEYE SAR satellite constellation is capable of providing 1-day repeat coverage observing at X-Band co-polarisation (https://www.iceye.com, last accessed 05.06.2023). ICEYE operates at different modes, including Stripmap and Spotlight Extended which provides data with a ground resolution in the order of 1 m. Building upon the achievements of the algorithm development in Glaciers_cci+ Phase 1 [RD2], within Glaciers_cci+ Phase 2 we adapted and evaluated the available algorithms based on both amplitude offset tracking and SAR interferometry (InSAR) to ICEYE data for ice surface velocity estimation of alpine type glaciers.

We considered ICEYE data already available at GAMMA over Scheelebreen (Svalbard) and Disko Island (Greenland) acquired within the Eurostars Project RAMON (Reference Number 113220, co-financed by Innosuisse). ICEYE tasking over Scheelebren (Figure 2.16, left) resulted in three series of 1-day acquisitions over 2 to 3 days in October 2021, December 2021 and January 2022 (Figure 2.17, left). ICEYE tasking over Disko Island (Figure 2.16, right) resulted in a series of 86 1-day acquisitions between 25 August 2021 and 30 December 2021 (Figure 2.17, right). The baselines of the ICEYE acquisitions at high latitudes are short (i.e. < 200 m) within a couple days, but they drift to considerably large values already after a few days. In the Disko Island dataset, however, the orbit control resulted again on small baselines after a couple of months.

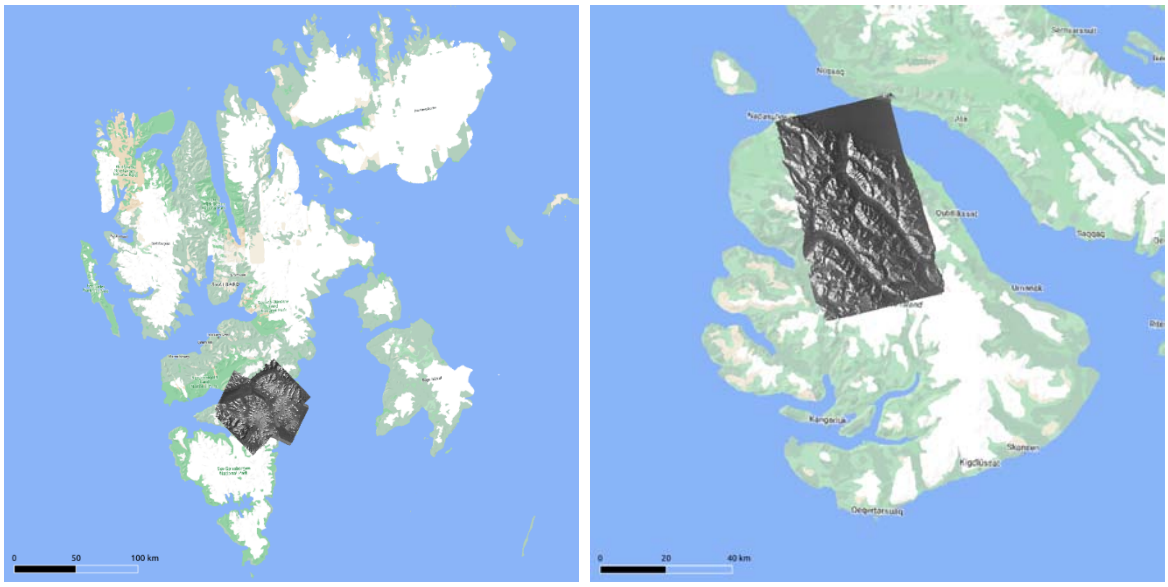

Figure 2.16: SAR backscatter images from ICEYE over the surging glacier Scheelebreen on Svalbard (left) and Disko Island, Greenland (right).

1 ref: 20211006 20211004 Bperp: 60.8 m delta_T: -2 days
2 ref: 20211006 20211005 Bperp: 33.6 m delta_T: -1 days
3 ref: 20211006 20211006 Bperp: 0.0 m delta_T: 0 days
4 ref: 20211006 20211007 Bperp: -40.6 m delta_T: 1 days

1 ref: 20211202 20211201 Bperp: -173.9 m delta_T: -1 days
2 ref: 20211202 20211202 Bperp: 0.0 m delta_T: 0 days
3 ref: 20211202 20211203 Bperp: 162.7 m delta_T: 1 days

5 ref: 20211006 20220102 Bperp:-4744.8 m delta_T: 88 days
6 ref: 20211006 20220103 Bperp:-4330.6 m delta_T: 89 days
7 ref: 20211006 20220104 Bperp:-3901.9 m delta_T: 90 days
8 ref: 20211006 20220105 Bperp:-3459.6 m delta_T: 91 days

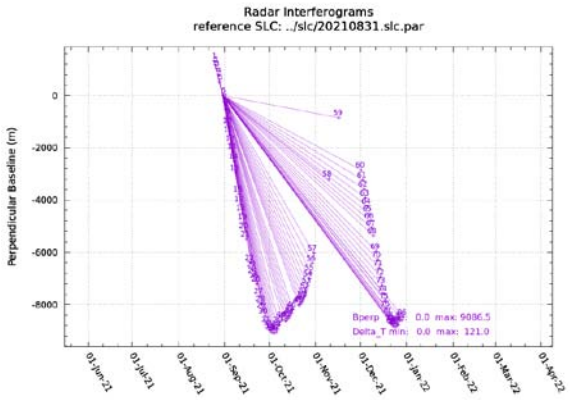

Figure 2.17: Perpendicular baseline distribution of the ICEYE data over Scheelebreen, Svalbard (left) and Disko Island, Greenland (right) as a function of the acquisition dates.

2.8.2 Methods

Available algorithms from Glaciers_cci+ Phase 1 [RD2] based on SAR interferometry (InSAR) and offset-tracking are adapted to ICEYE data for ice surface velocity estimation of alpine type glaciers. For InSAR we considered data acquired with 1-day repeat cycle and stable surface conditions in winter. Offset-tracking was tested for all available data and repeat cycles of several days. The product quality is assessed by intercomparison with ice velocity products from Sentinel-1.

The InSAR processing consists of co-registration the SLC acquisitions, generating a phase image, subtracting the flat earth and topographic phase contributions, phase unwrapping, calibration based on slow-moving ice-free areas and subsequently conversion into line-of-sight velocity. Provided that coincident velocity measurements from at least two different viewing geometries (i.e. two different heading angles) are available for a given point, the three-dimensional velocity components can be determined. However, this is not the case for the available ICEYE data, which only allowed computation of the line-of-sight velocity.

Offset-tracking procedures allow to compute three-dimensional ice surface displacement maps combining the slant-range and azimuth offsets by assuming that flow occurs parallel to the ice surface as estimated from a DEM (e.g. Strozzi et al. 2002)). The offset-tracking processing lines available from the previous phases of the project are adapted to the format of the ICEYE data. Ice surface velocity maps from ICEYE are then compared to Sentinel-1 results.

2.8.3 Processing line

The InSAR processing line is depicted in Fig. 4.2 of [RD2]. Although this processing line is designed for Sentinel-1 TOPSAR acquisitions, it was straightforward to adapt it to ICEYE data. As an example, the ICEYE interferogram over 1 day for 2021.12.24 to 2021.12.25 after phase calibration is shown in Figure 2.18 along with a 6 day Sentinel-1 interferogram for 2021.12.15 to 2021.12.21. Baselines are in both cases very small, -5 m for ICEYE and 30 m for Sentinel-1. Fringes are well preserved in both cases, but phase unwrapping of the ICEYE interferogram is more straightforward because of the smaller number of fringes.

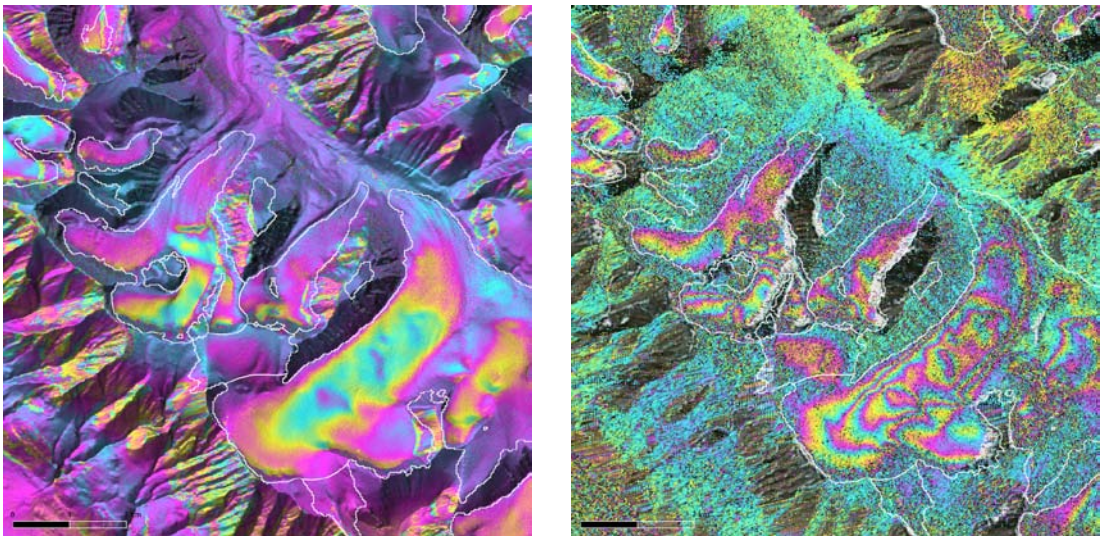

Figure 2.18: ICEYE 1-day differential interferogram from 2021.12.24 to 2021.12.25 (left) and Sentinel-1 6-day differential interferogram from 2021.12.15 to 2021.12.21 (right) for part of Disko Island (Greenland). Ice divides (white) are from RGI 5.0.

The offset-tracking processing line is depicted in Fig. 4.11 of [RD2]. The generalised processing line for offset-tracking could be adapted to ICEYE data, which are distributed in SLC (Level 1) format, without significant problems. Taking into consideration the slant range pixel spacing of 1.15 m, the local incidence angle of 35° and the azimuth pixel spacing of 1.55 m, tracking was employed with window sizes of 96 x 128 pixels, i.e. a dimension on the ground of 192 m x 198 m. The steps in slant range and azimuth direction were 12 and 16 pixels, respectively, i.e. 24 m x 25 m.

As an example, the ice velocity map for Scheelebreen from ICEYE over 1 day for 2022.01.04 to 2022.01.04 is shown in Figure 2.19 along with a 12 day Sentinel-1 ice velocity map for 2021.12.28 to 2022.01.09. The ICEYE result shows a much better displacement field than Sentinel-1 as a consequence of the smaller image template sizes that can be used for tracking for this relatively narrow glacier and the shorter time interval (1 day versus 12 days). In this case, 96.9% of valid points on ice were successfully tracked and the velocity mean and standard deviation over ice-free regions are 0.41 m/day and 0.78 m/day. The ice surface velocities estimated from Sentinel-1 are nearly everywhere strongly underestimated and there are also large areas without information, as previously observed over Himalayan glaciers with a width of about 1 to 2 km. ICEYE offers therefore the opportunity of a continuous, all-year around monitoring of ice surface velocity also for relatively narrow surging glaciers.

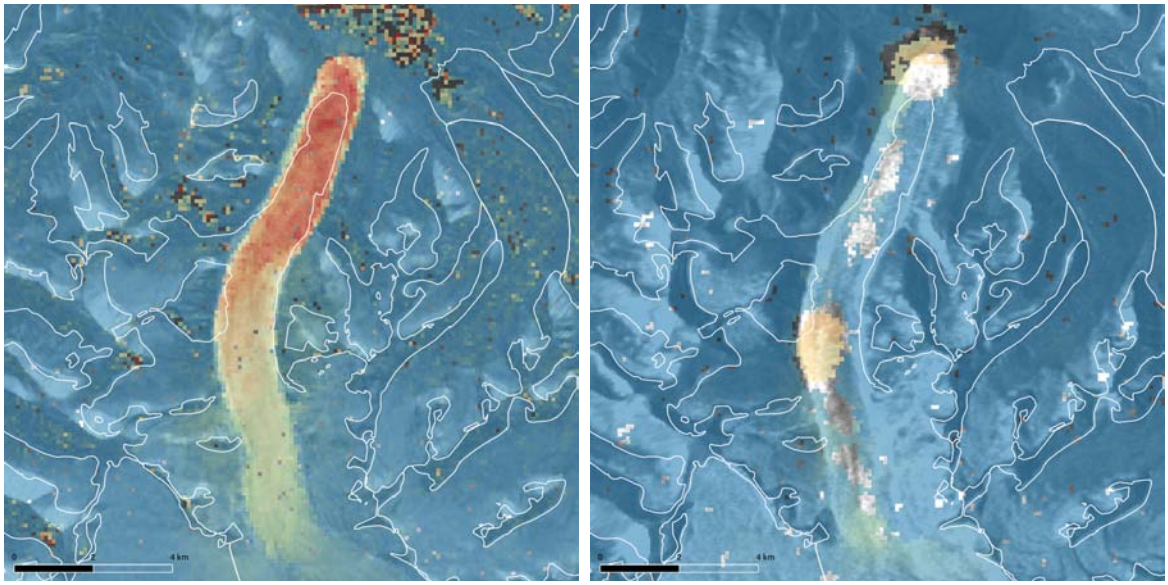

Figure 2.19: Ice velocity maps for Scheelebreen (Svalbard) from ICEYE over 1 day for 2022.01.04 to 2022.01.04 (a) and from Sentinel-1 over 12 days for 2021.12.28 to 2022.01.09. Ice divides (white) are from RGI 5.0. The colour scale is saturated at 2500 m/year (6.84 m/day).

3. Glacier Facies Mapping

3.1 Optical Sensors

3.1.1 Introduction

Glacier facies, including snow from the last winter season, firn (snow remaining from previous years but not yet converted to glacier ice - if applicable), clean glacier ice, and debris covered glacier areas can be classified from optical satellite data based on the differences in their spectral reflectance properties.

Of main interest is the snow remaining on glaciers at the end of the ablation season (e.g., Rabatel et al. 2017, Barandun et al. 2018), building the accumulation area of a glacier. As snow can fall all around the year on glaciers in the Karakoram region and glaciers in optical satellite images are frequently obscured by cloud cover, the classification of glacier facies from optical satellite data is based on time series of Sentinel-2 or Landsat scenes acquired during the melting period. A high-resolution digital elevation model (DEM), atmospheric parameters from reanalysis data, and glacier outlines are needed as auxiliary data for the classification. The Copernicus GLO-30 DEM and the SRTM V4 DEM are both covering the full Karakoram region without any data gaps, and are used to investigate the impact of the DEM's resolution and timing on the pre-processing chain applied to account for topographic effects, such as cast shadow estimations.

3.1.2 Methods

The method for the glacier facies classification from Sentinel-2 and Landsat data was developed by ENVEO within the ESA EXPRO+ AlpGlacier project for glaciers in the Alps (cf. ESA EXPRO+ AlpGlacier ATBD v2), and is adapted for the glaciers in the Karakoram.

The processing chain starts with the automated download of Sentinel-2 and Landsat data for a pre-defined area of interest, allowing a maximum cloud coverage of 30% per scene for the search criteria. After downloading, the spectral reflective bands required for the further processing are imported and converted to top of atmosphere reflectances.

Clouds are masked using sensor-specific algorithms or available cloud masks. For Sentinel-2 scenes, the python module "s2cloudless" is used to mask clouds. This tool requires the top of atmosphere reflectance data of 9 spectral bands (B01, B02, B04, B05, B08, B8A, B09, B10, B11, B12), all prepared in the same grid spacing. To avoid additional resampling, all of these spectral bands are prepared at 10 m pixel spacing. For Landsat data, the cloud mask with "HIGH PROBABILITY" of the L2A products is used.

The spectral reflectance data required for the GLF classification are corrected for atmospheric and topographic effects. For the atmospherically corrected bottom of atmosphere reflectance data provided by Copernicus and USGS as L2A products, different radiative transfer models and additional processing steps are used. To allow the same GLF classification rules for the data from different sensors, we apply a homogenised pre-processing procedure to all input data, including the correction of cast shadow effects. The radiative transfer (RT) model 6S (Second Simulation of a Satellite Signal in the Solar Spectrum) (Vermote et al., 1997, 2006) is used for the calculation of the radiative fluxes. The standard atmospheric correction as-

sumes a horizontal target. Thus, the RT model is executed for multiple target heights, stored in LookUp Tables (LUTs). For each pixel, the different contributions to the solar illumination are then linked to the surface height using a DEM. In cast shadowed areas, the total solar irradiance is only built by diffuse and terrain illumination contributions. To avoid under- or over-corrections, cast shadowed areas need to be identified before calculating the total solar fluxes per pixel. For the estimation of the cast shadowed areas, terrain parameters derived from the DEM are combined with the spectral top of atmosphere reflectance per scene to allow shadow detection visible in the scene but not detectable from the DEM, e.g. due to the flattening of the terrain at the available pixel spacing. The approach of Sandmeier and Itten (1997) is used to calculate the bottom of atmosphere reflectance per pixel, correcting for the local illumination conditions.

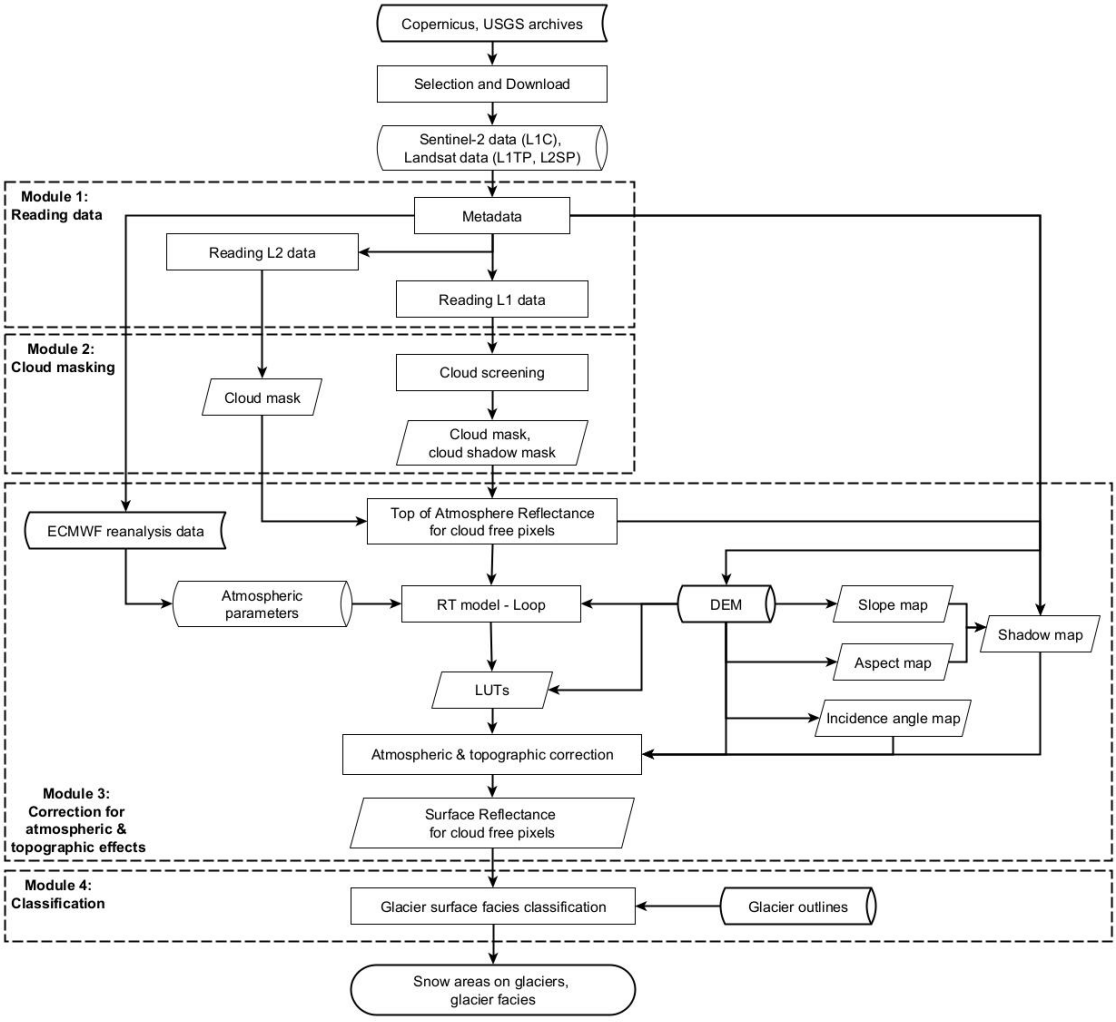

Figure 3.1: Processing line for the glacier facies classification from Sentinel-2 and Landsat data.

The resulting spectral bottom of atmosphere reflectances are used for the GLF classification. The corrected reflectances are tailored to the glacier areas using glacier outlines (e.g. RGIv6.0, region 14 for South Asia West). The glacier outlines have to be prepared in the same map projection as of the satellite data, i.e. in UTM43/WGS84 map projection. The tailored spectral reflectance data are statistically analysed to identify any local minima in the value distributions, which can be used as a starting point for the separation of snow and ice areas. A series of rules organised in a hierarchical structure are then applied to the tailored

spectral reflectance data to classify snow areas remaining from the last winter season, firn areas (if applicable), clean glacier ice areas, and debris covered glacier areas. The classification rules are iteratively adjusted, starting with classifications with a low uncertainty towards the classification of pixels with ambiguous spectral reflectance conditions, resulting in a classification with a high uncertainty. Clouds are masked in the final product.

The cloud screening and the pre-processing steps are performed per scene. For the GLF processing, in particular for the identification of firn areas, time series per tile are analysed. Any geometric displacements in overlapping satellite scenes can thus result in misclassifications in the GLF classification. Such shifts are also affecting the merging of GLF products from neighbouring satellite scenes. The cloud masks for Sentinel-2 and Landsat scenes are usually affected by either a cloud or a no-data boundary of a few pixels outlining the scene. Before merging the GLF products from neighbouring scenes, the maps need to be cropped by a few pixels to avoid cloud or no-data features along the boundaries of overlapping scenes.

3.1.3 Processing line

The detailed processing chain for the glacier facies classification from Sentinel-2A/B or Landsat data is shown in Figure 3.1.

3.2 SAR sensors

3.2.1 Introduction

SAR sensors, such as Sentinel-1 or ICEYE, supporting co-polarised and dual polarised SAR data allow the classification of the wet snow extent on glaciated areas during the melting season. Repeat pass SAR data for at least one winter season are required as input to prepare a reference backscatter map at cold and dry snow conditions which is used as input for the wet snow classification.

A DEM is needed for the geolocation of the SAR data, and glacier outlines support the classification focusing on the glacierized areas. Information from the optical satellite data can support the removal of heavily crevassed glacier areas to avoid misclassifications from the SAR data.

3.2.2 Methods

The classification of wet and dry snow areas on glaciers from SAR data is based on a threshold applied to the ratio of backscatter coefficients from the scene of interest, and a backscatter reference image generated from time series of SAR acquisitions from the main winter season when the snow and ice areas are cold and dry. The approach is based on the method of Nagler et al. (2016), but is adapted for the wet snow classification on glaciated areas in the Karakoram.

Glacier areas in the radar layover, foreshortening, or radar shadow are masked.

3.2.3 Processing line

The processing line for the wet snow detection on glaciers from SAR data is shown in Fig. 3.2.

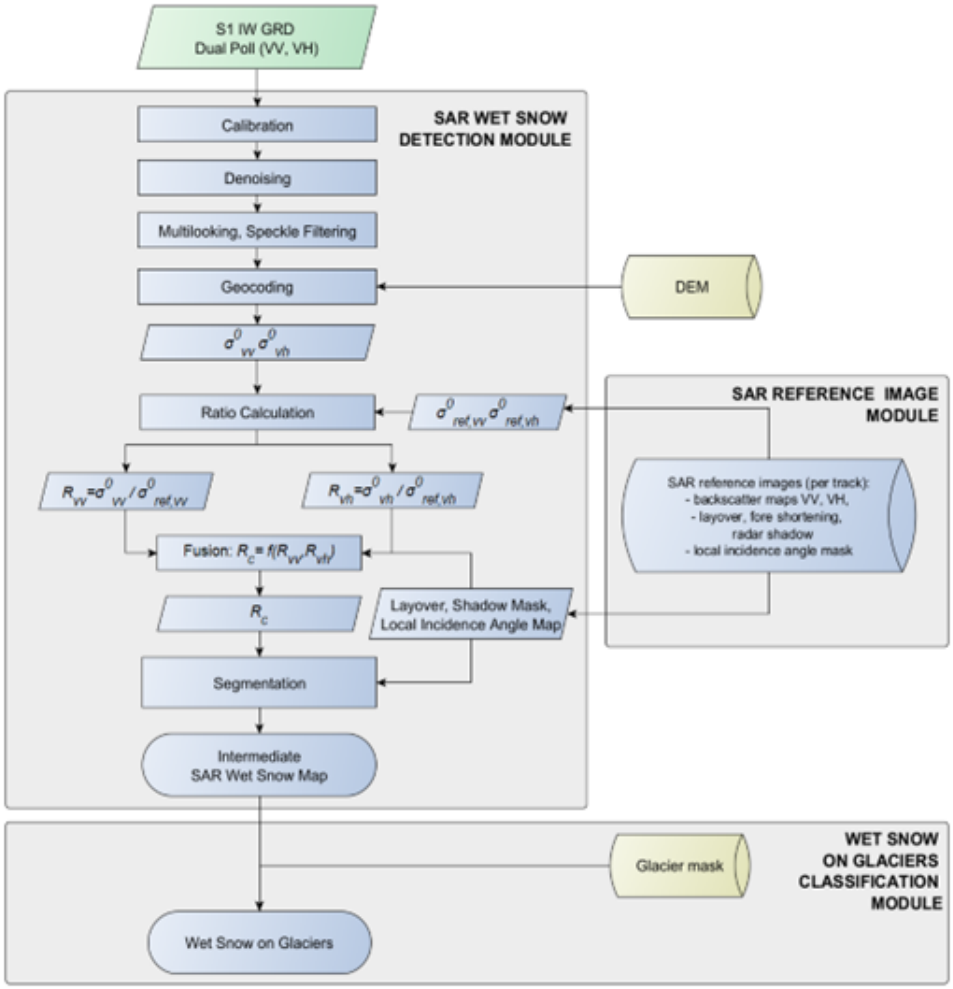

Figure 3.2: Processing chain for the wet snow classification on glaciers from SAR data.

4. Glacier surge detection

4.1 Backscatter differences from Sentinel-1

4.1.1 Introduction

The here-presented method to detect and inventory glacier surges is based on variations in the strength of radar backscatter over time. As a surge implies substantial increase in the flow velocity and velocity gradients of a glacier, the glacier surface typically becomes more crevassed and radar backscatter is increased during an active surge (Copland et al., 2003, Grant et al., 2009). Likewise the glacier surface will become less crevassed and therefore the backscatter will decrease at the end of an active surge phase. Glacier crevasses represent strong surface roughness for incoming radar waves, with rectangular shapes and even side walls, and radar backscatter is thus typically stronger over crevasses than for most other glacier surface types. Comparison of the radar backscatter strength between two time intervals, i.e. investigating whether backscatter increases or decreases with time, therefore helps to detect the build-up or decay of glacier surges. Thereby, the weather and daylight independence of SAR data offers the opportunity for highly systematic surveys and a flexible choice of the time intervals to compare. Here, we exploit annual changes in surge activity, noting that shorter or longer time intervals might also be of interest for certain applications. As a backbone for our surge detection and inventorying we use radar backscatter imagery from the EU ESA Copernicus Sentinel-1 C-band mission that has provided data with potential global coverage since its launch in April 2014. The actual Sentinel-1 coverage depends on the acquisition plan, meaning that certain areas of interest may have infrequent coverage. In a further step, we extend surge detection and inventorying back in time, beyond 2014/2015 using previous SAR missions such as Envisat ASAR and JERS (see following Section 4.2).

4.1.2 Methods

The increase in crevassing that is typically associated with surge-type glacier instabilities often causes strongly enhanced radar backscatter in satellite SAR images. This signal can be enhanced by stacking repeat radar images, preferably taken from the same nominal orbit to avoid variation of topographic effects and taken over the winter season, when glaciers typically show little other backscatter change due to cold and dry conditions. A synthetic image of strongest backscatter is then created over each seasonal (or sub-seasonal) stack (Figure 4.1). When comparing these individual stack maximum images over different years, for instance using normalised differences, the so-called normalised difference index (NDI), increased crevassing appears in our implementation bright in the grey-scaled NDI image between two years, decreasing crevassing appears dark, and areas of moderate change appear medium grey (Equation 4.1; Figure 4.1).

$$NDI_{\ maxGRD\ yr2-yr1} = \frac{(maxGRD\ yr2 - maxGRD\ yr1)}{(maxGRD\ yr2 + maxGRD\ yr1)} \quad (Eq.\ 4.1)$$

The spatial patterns of such backscatter increases or decreases are then visually interpreted to decide whether they indicate glacier surges, or other changes not of interest here (*Figure 4.2)*. The method is easily applied to SAR data held on remote servers or locally. For demonstration we apply the approach here to the Sentinel-1 C-band data archive as available in Google Earth Engine (Gorelick and others, 2017) and use this cloud-processing platform to generate winter backscatter NDI images and manually mark the locations of surge-type events.

This approach was recently introduced by Leclercq and others (2021), including the code, tests of a number of parameterizations, and validation against measured velocity time series.

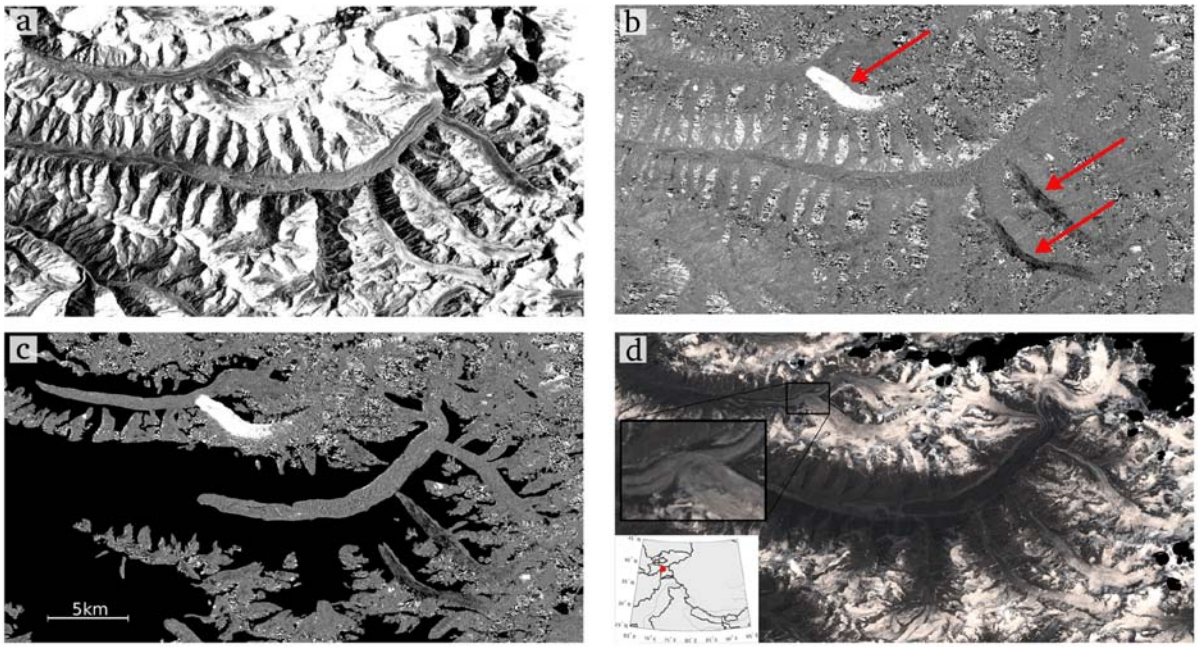

Figure 4.1: Example for detecting glacier surges from differencing backscatter stack maxima of different winter seasons for a glacierized area surrounding the Obihingo (also called Obikhingou) river basin in the central Pamirs, Tajikistan. (a) Aggregated Copernicus Sentinel-1 maximum backscatter winter 2018. (b) Normalized Difference Index (NDI) image from Sentinel-1 maximum backscatter winter 2018–winter 2019. Arrows indicate areas with increased and decreased radar backscatter over glaciers: Gando Glacier, Vanchdara Glacier, and Shocalscogo Glacier, from top to bottom. (c) NDI image 2018–2019 masked with GLIMS glacier outlines. (d) Copernicus Sentinel-2 optical image summer 2019, with cloud mask in black and zoomed-in view of the protruding in the main trunk of Gando Glacier; inset shows the location of the images.

A number of modifications and different parameterisations of the method are easily implemented and the optimal combination might vary from region to region, depending on available data (e.g. polarisation, ascending/descending), topography (e.g. layover, forshortening and radar shadow effects), and glacier seasonality (i.e. which seasons show stable backscatter). Also the annual stack statistics applied might be varied, e.g. median, stack maximum backscatter or percentile. We find that cross-polarisations (VH and HV) perform often well, but in some cases co-pol (HH or VV) works at least as good. It can facilitate interpretation if several parameter combinations are computed and viewed simultaneously, for instance the NDIs from both ascending and descending paths over the same area, or different polarisations (if available). Typically, NDI images are built from subsequent winters, but also pluri-annual time differences can be useful. For better visualisation, final NDI images are noise-filtered, for instance using a 3x3 median filter.

We also find that stacking the individual annual NDIs, animating the stack, and/or visualising the minimum or maximum of the entire multiannual NDI stack supports initial detection of surges (F*igure 4.2*).

We apply the method to calibrated and orthorectified Ground Range Detected (GRD) data within Google Earth Engine (GEE), but note that the NDI used makes the method robust and applicable to any other GRD processing level as long as the same nominal orbits are compared.

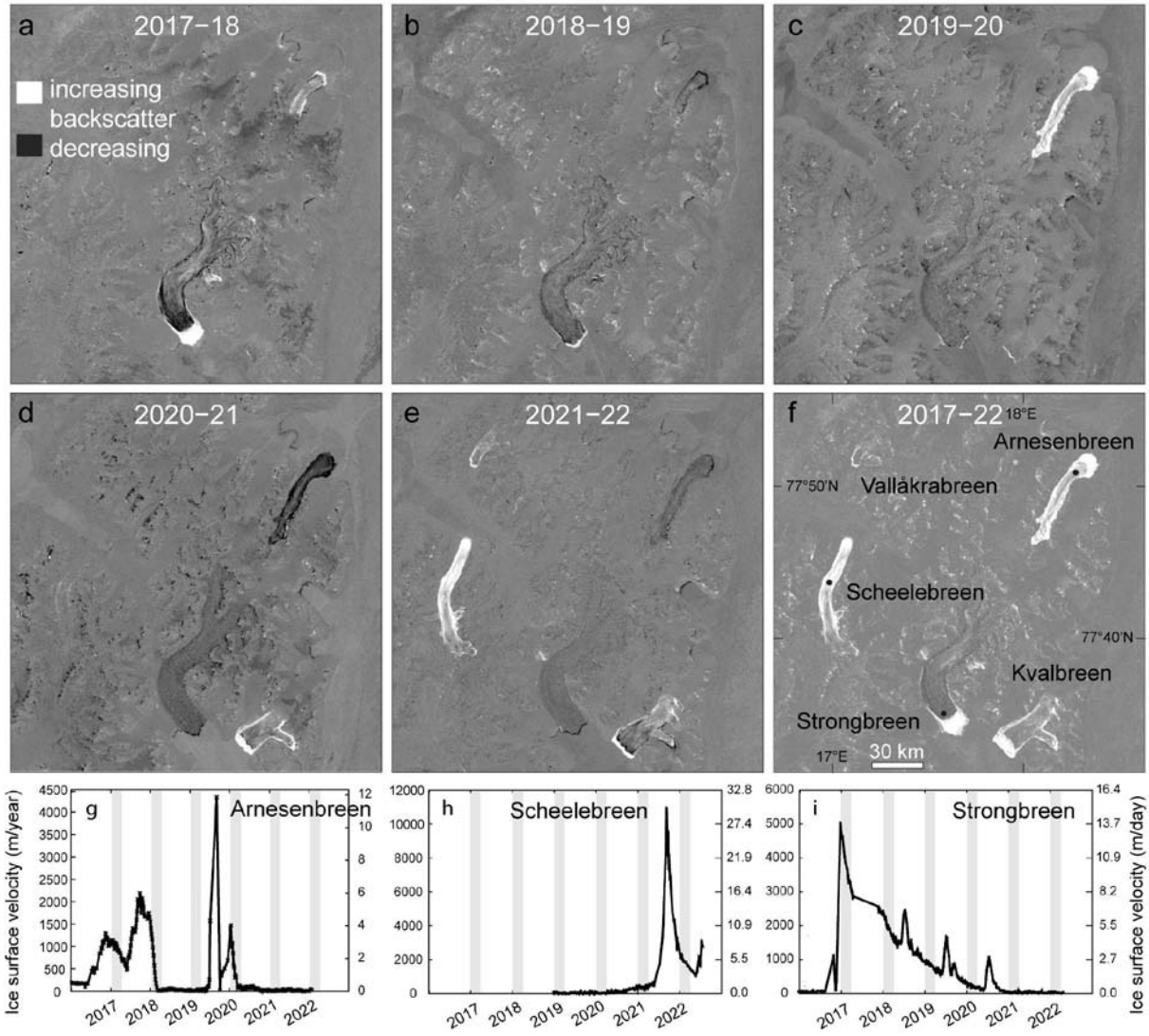

Figure 4.2: Examples of winter-to-winter Sentinel-1 radar backscatter changes for a region in south-east Spitsbergen, displayed as normalised differences between maximum winter backscatter of two subsequent years (a-e). Bright regions indicate increasing backscatter, dark regions decreasing backscatter over time. The former is interpreted as increasing crevassing and surge-type activity, and vice-versa. The middle right panel (f) shows the maximum backscatter normalised difference over the entire five-year period and indicates the five surges observed in the area. The lowest row (g-i) shows selected comparisons to glacier surface velocity time series. The grey vertical bars in the panels of the lowest row indicate the periods over which Sentinel-1 data have been stacked for examples a-f (1 Jan – 1 Apr of each year). Velocity series g-i refer to single points on the surge centre (black dots in panel f).

Within GEE the following pre-processing is applied (http://https://developers.google.com/earth-engine/guides/sentinel1):

Level-1 Ground Range Detected (GRD) Sentinel-1 scenes are processed to backscatter coefficient (σ°) in decibels (dB). GEE uses the following pre-processing steps (using and as implemented by the ESA Sentinel-1 Toolbox within SNAP) to derive the backscatter coefficient in each pixel:

1. Apply orbit file: Updates orbit metadata with a resituated orbit file (or a precise orbit file if the resituated one is not available).
2. GRD border noise removal: Removes low intensity noise and invalid data on scene edges (as of January 12, 2018).
3. Thermal noise removal: Removes additive noise in sub-swaths to help reduce discontinuities between sub-swaths for scenes in multi-swath acquisition modes. (This operation cannot be applied to images produced before July 2015).
4. Application of radiometric calibration values: Computes backscatter intensity using sensor calibration parameters in the GRD metadata.
5. Terrain correction (orthorectification): Converts data from ground range geometry, which does not take terrain into account, to σ° using the SRTM 30 m DEM or the ASTER GDEM for high latitudes (greater than 60° or less than -60°).

4.1.3 Processing line

The processing line of detecting surges from SAR backscatter changes is given in Figure 4.3.

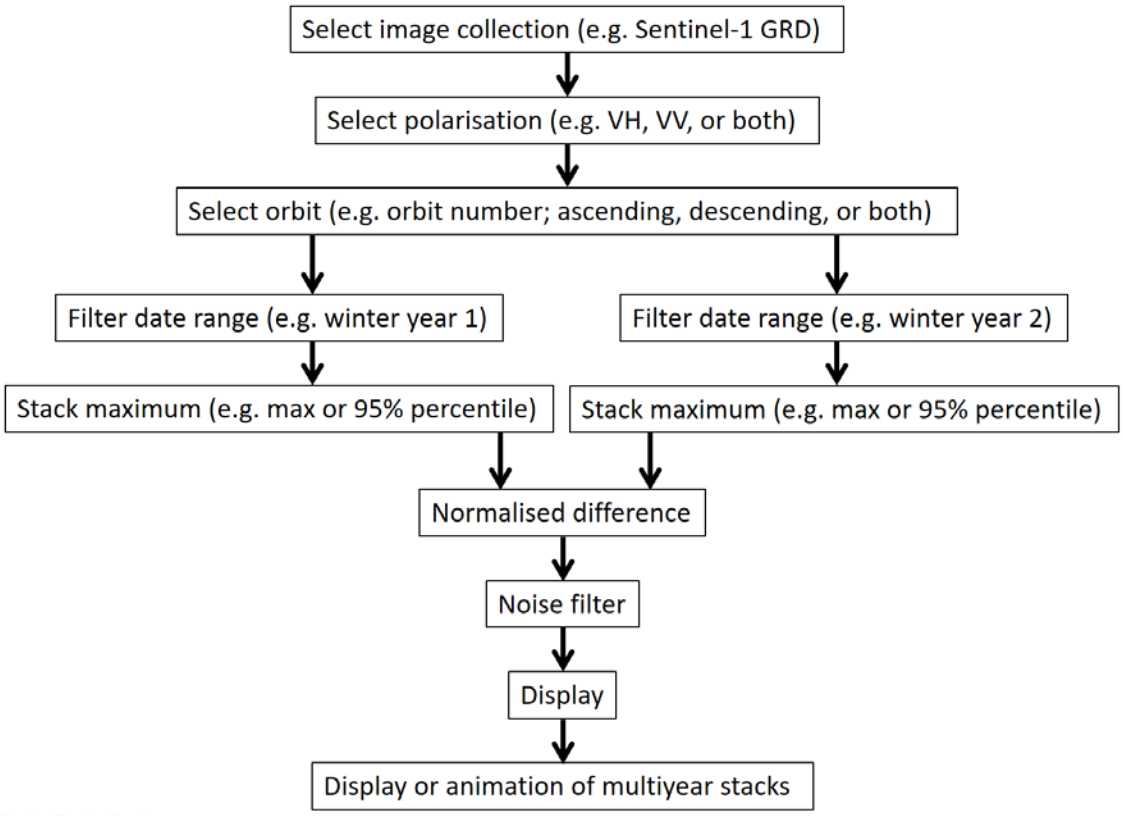

Figure 4.3: Processing line to compute inter- or pluri-annual difference images of winter-to-winter SAR backscatter differences for surge detection.

4.2 SAR backscatter image time series from sensors other than Sentinel-1

4.2.1 Introduction

The Sentinel-1 based inventory of recent glacier surges that is based on variations in the strength of radar backscatter over time will be extended in both space and time using other satellite radar sensors, e.g. ERS-1/2 (1991-2011), JERS-1 (1992-1998), Radarsat-1 (1995-2013), ENVISAT ASAR (2002-2012), ALOS-1 PALSAR-1 (2007-2011), Radarsat-2 (2007-present) and ALOS-2 PALSAR-2 (2014-present).

In particular, GAMMA already processed all the ENVISAT ASAR Image Mode (IM), Wide Swath Mode (WSM) and Global Monitoring Mode (GMM) data available on ESA's G-POD as part of CCI Land Cover to 150 m resolution. These data have been used in a series of projects including Globbiomass, CCI Biomass and CCI Land Cover (e.g. Santoro et al., 2015 and 2021) and 1° x 1° tiles of normalised SAR backscatter after multi-temporal speckle filter can be used to produce additional regional or global glacier surge inventories.

In addition, in a project funded by the Japanese Space Agency JAXA, GAMMA processed the global archive of JERS-1 L-band SAR data acquired between mission launch in 1992 and the end of the mission in 1998 to radiometric-terrain-corrected (RTC) level data. JAXA provided access to 478447 images in Level 0 raw format that were available in JAXA's archives. The target requirements were defined by JAXA as listed below:

1. 20 m x 20 m equivalent resolution in geographic spatial reference system (0.000222° x 0.000222°);
2. processing to radiometric-terrain-corrected gamma nought HH polarization backscatter intensity;
3. backscatter images shell be accompanied by local incidence angle maps, layover/shadow maps, and CARD4L compliant XML files containing summaries of the most relevant information about the imagery and pre-processing;
4. delivery of all imagery in form of 1° x 1° tiles in cloud-optimized Geotiff format.

4.2.2 JERS-1

The flowchart in Figure 4.4 provides an overview of the processing workflow that was implemented based on the GAMMA software. The processing was organised on a per-orbit basis, i.e., all L0 images acquired from the same orbit were processed simultaneously. For each of the raw images the processing included:

1. Focussing to Single Look Complex (SLC) format including filtering for radio frequency interference (RFI) effects, antenna gain corrections, as well as corrections for the noise floor;
2. 2 x 7 multi-looking in range and azimuth, respectively, to obtain multi-look intensity images (MLI) with a ground range pixel posting of about 25 m;
3. calculation of transformation functions (so called geocoding look-up tables) for resampling between slant-range and map geometry based on the available orbit information and the global ALOS-1 PRISM DEM AW3D30 (https://www.eorc.jaxa.jp/ALOS/en/dataset/aw3d30/aw3d30_e.htm) with 1 arc-second resolution;
4. calculation of maps of the local incidence angle and layover/shadow masks;
5. refinement of the geocoding look-up tables (discussed in more detail below);

6. pixel area normalization as with Frey et al. (2013) to obtain radiometrically and terrain-corrected gamma nought backscatter images;
7. resampling to the target map geometry in geographic spatial reference system based on the refined geocoding look-up tables.

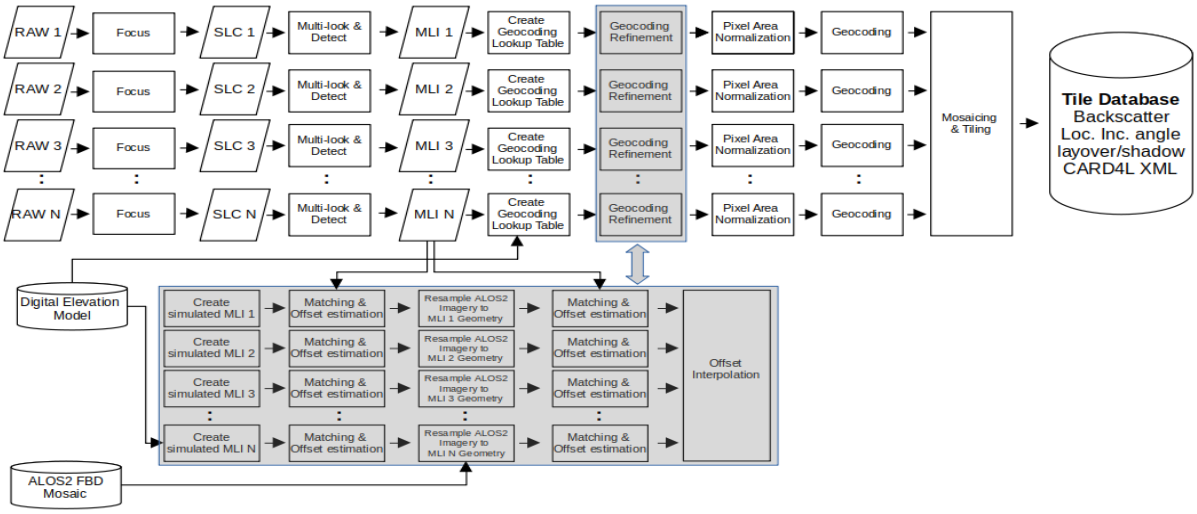

Figure 4.4: Workflow for processing one orbit of JERS-1 L0 imagery to RTC level.

In the case of more recent satellite SAR missions such as Sentinel-1 or TerraSAR-X, the accuracy of the orbit information is generally high enough for the imagery to be geocoded with high spatial accuracy using the initial geocoding look-up table without further corrections. However, in the case of JERS-1 further refinement of the look-up table is required. Existing assessments of the accuracy of the orbit information available for JERS-1 indicated errors resulting in offsets of several tens of meters in range and 100 m in azimuth (Shimada and Isoguchi, 2002). Our own analysis in few cases even indicated offsets in azimuth reaching several kilometres. That is why, an iterative refinement procedure had to implemented for processing all available JERS-1 images to the highest possible spatial accuracy.

In the refinement of the geocoding look-up table, a simulated backscatter image is calculated from the DEM and subsequently resampled to the slant-range geometry of the respective MLI. A cross-correlation between small image chips distributed evenly across the simulated image and MLI is then performed to identify offsets in range and azimuth and to calculate polynomials describing the variation of offsets along the range and azimuth dimensions of the MLI. The polynomials are then used to update the geocoding look-up table. Since based on a DEM only, the simulated SAR image that serves as reference only presents topographic features. In areas without topography, a refinement is therefore not possible. In such cases, an existing 20 m resolution ALOS-2 PALSAR-2 Fine-Beam Dual-polarization (FBD) L-band HH polarization backscatter dataset released by JAXA in the form of global mosaics (Shimada and Ohtaki, 2010; Shimada et al., 2014) served as geometric reference for the refinement.

JAXA also has released mosaics produced from ALOS-1 PALSAR-1 FBD imagery for the years 2007 to 2010, i.e., data acquired closer to the time frame of the JERS-1 acquisitions. However, we here selected the ALOS-2 2018 mosaic as reference because the mosaic had recently been reprocessed with high geolocation accuracy whereas the ALOS-1 mosaics are known to present significant geolocation offsets locally. The corresponding subset in the

ALOS-2 HH polarization mosaic was resampled to the slant-range geometry of the JERS-1 MLI and the cross-correlation was performed again to identify the offsets.

A refinement of the geocoding look-up table based on cross-correlation either against a simulated SAR image or the ALOS2 FBD imagery allowed for accurate geocoding of 258629 JERS-1 frames. The geocoding accuracy was generally of the order of 2 m in range and azimuth, respectively. For the rest of the images, however, offsets had to be interpolated from adjacent frames acquired from the same orbit for which the refinement procedure described above produced accurate offset estimates. Due to the relatively small changes of the offsets in range and azimuth between adjacent frames acquired along the same orbit, high geospatial accuracy at sub-pixel level can still be achieved even when having to interpolate offsets across consecutive frames. However, primarily in the Antarctic a refinement of the geocoding look-up tables was often not possible due to:

1. the temporal mismatch between the AW3D30 DEM, which was produced from imagery acquired more than 10 years after the acquisition of the JERS-1 imagery, thus no longer representing the extent/location of many glaciers in the time frame of the JERS-1 acquisitions;
2. the lack of L-band imagery in the JAXA ALOS-1 PALSAR-1 and ALOS-2 PALSAR-2 FBD mosaics over the Antarctic continent, which is why the geocoded JERS-1 imagery in those areas may present large geolocation errors.

Following the geocoding of all JERS-1 backscatter images, the processing concluded with the mosaicking of all geocoded backscatter images from the same orbit and the creation of 1° x 1° tiles of the backscatter as well as the corresponding local incidence angle and layover/shadow maps. The tiled imagery were stored as either 16-bit (backscatter, local incidence angle) or 8-bit (layover/shadow map) cloud-optimized Geotiffs. To be able to store the backscatter images as 16-bit integer files, they were converted to amplitude scale. Linear power values may be obtained from the digital numbers (DN) reported in the files with:

$$\gamma = 10^{\left((20 * \log_{10} DN - 83)/10\right)} \quad (Eq.\ 4.2)$$

For each individual tile, the final database includes an xml file summarising the information about the imagery and pre-processing most relevant for users. The xml files were produced following CEOS CARD4L standards (https://ceos.org/ard/files/PFS/NRB/v5.5/CARD4L-PFS_Normalised_Radar_Backscatter-v5.5.pdf). The xml files also include information about the geocoding accuracy achieved for the particular image.

At global scale, we find the best coverage over Northern Europe, Eastern Asia, and Southeastern Asia (*Figure 4.5*), which can be explained with the location of receiving stations. Throughout the seven years of operation, JERS-1 was able acquire an almost complete global coverage, i.e., each area was covered at least once. In contrast to more recent spaceborne SAR missions, however, no systematic acquisition plan had been defined for JERS-1, which is why land areas were not covered systematically on an annual basis (*Figure 4.6*), but rather in the frame of mission phases dedicated to cover certain areas once or repeatedly from consecutive JERS-1 orbital cycles; note that JERS-1 was flown in a 44 days repeat orbit.

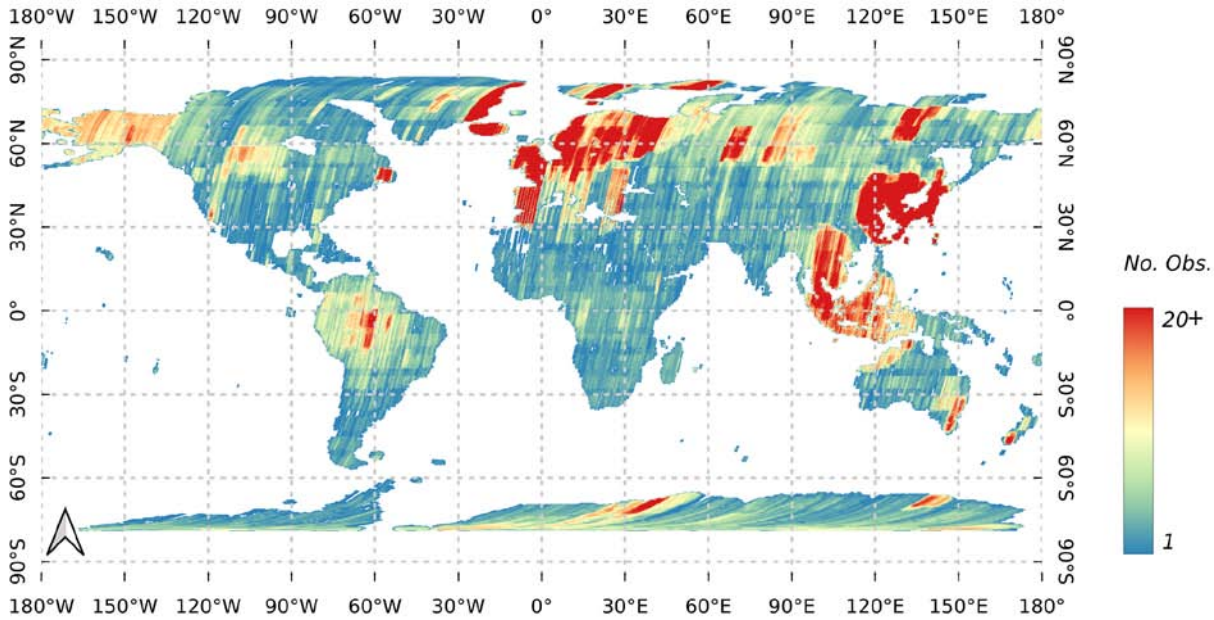

Figure 4.5: Number of images acquired by JERS-1 between 1992 and 1998.

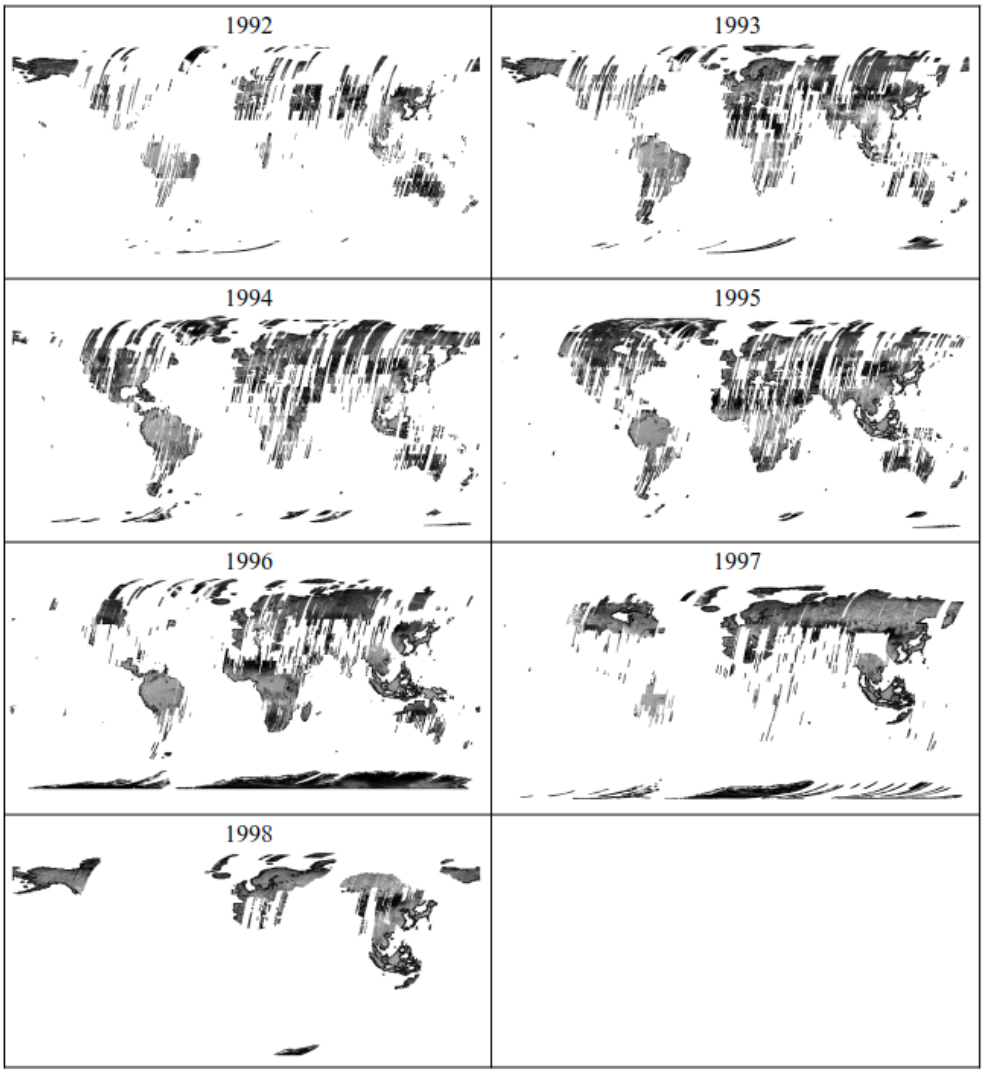

Figure 4.6: Annual coverage of JERS-1 between 1992 and 1998.

4.2.3 ENVISAT ASAR

The processing of the ENVISAT ASAR Image Mode (IM), Wide Swath Mode (WSM) and Global Monitoring Mode (GMM) data available on ESA's G-POD performed by GAMMA as part of CCI Land Cover to 150 m resolution is described in Santoro et al. (2015). Processing was implemented to obtain calibrated and speckle filtered images with sub-pixel co-registration accuracy, arranged in a structure that allowed for easy access and man agreement (Santoro et al., 2011). To this end, a global grid tied to the geographic reference system and having its origin at 90° N, 180° W, with tiles of relatively small size (1° × 1°) was used. To adhere with the pixel size of the WSM and IMM images, the GM1 images were oversampled to 150 m. As a result of the SAR processing, the dataset of ASAR backscatter observations to be used for classification originated solely from images acquired in WSM mode for the majority of the Earth land surfaces, with a few complements locally from IMM data. North of 60° N and over large parts of Europe, more than 300 observations per pixels were common. For approximately 3% of the area mapped, corresponding to northern Greenland, Svalbard and the Arctic isles of Russia, more than 1000 observations were available.

4.2.4 Method and Processing line

The method and processing line implemented to detect glacier surges from Sentinel-1 backscatter differences are described in Section 4.1.2 and 4.1.3. Stacking repeat radar images, preferably taken from the same nominal orbit and over the winter season, is proposed to improve the detection of the backscatter increase or decrease and the NDI is computed. The spatial patterns of such backscatter increases or decreases are then visually interpreted to decide whether they indicate glacier surges or other changes.

The method is easily applied to other SAR data, with a number of modifications and different parameterisations of the method that can be easily implemented depending on available data (e.g. polarisation, ascending/descending, number of acquisitions, etc.). For JERS-1, for instance, we found that seasonal and annual voids in JERS-1 holdings require more intervention in the selection of periods to compare and that the L-band penetration and lower resolution make identification of surges more tricky than using C-band because changes other than from surges can produce similar patterns of backscatter changes (*Figure 4.7*). In addition, out-of-date DEMs had to be used for terrain correction and the resulting correction artefacts may introduce apparent changes (e.g. at much changed calving fronts).

Finally, some of the JERS-1 tiles do show errors in the calibration in the form of bright stripes, which are due to erroneous information on the automatic gain control that could not be corrected for in the processing. *Figure 4.8* illustrates an example of tiled backscatter imagery for an area in Germany (10°-11° E, 49°-50° N). In total, 79 images acquired between 1993 and 1997 (partially) cover the particular tile, with the scenes from 19980110, 19920624 and 19950106 showing errors in the calibration. As a result more care is needed for surge identification and small/weak surges are harder to detect, or cannot be detected.

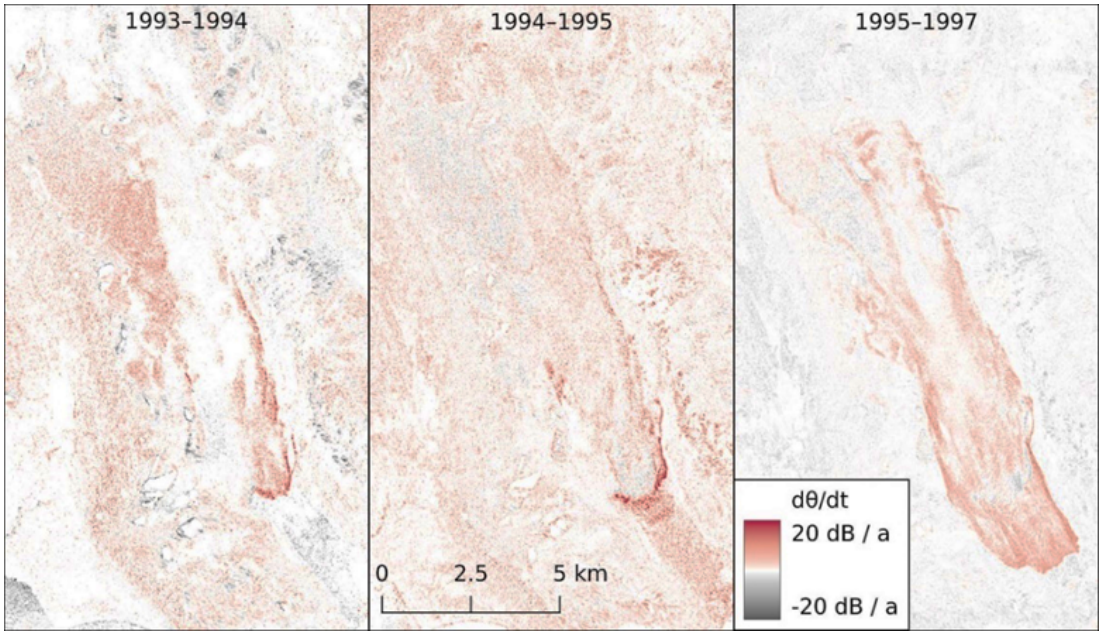

Figure 4.7: Example of winter-to-winter JERS-1 radar backscatter changes for Fridtjovbreen, Svalbard, displayed as normalised differences between maximum winter backscatter of subsequent years. Red indicates increasing backscatter, grey decreasing backscatter over time. Increasing backscatter is interpreted as increasing crevassing and surge-type activity, and vice-versa.

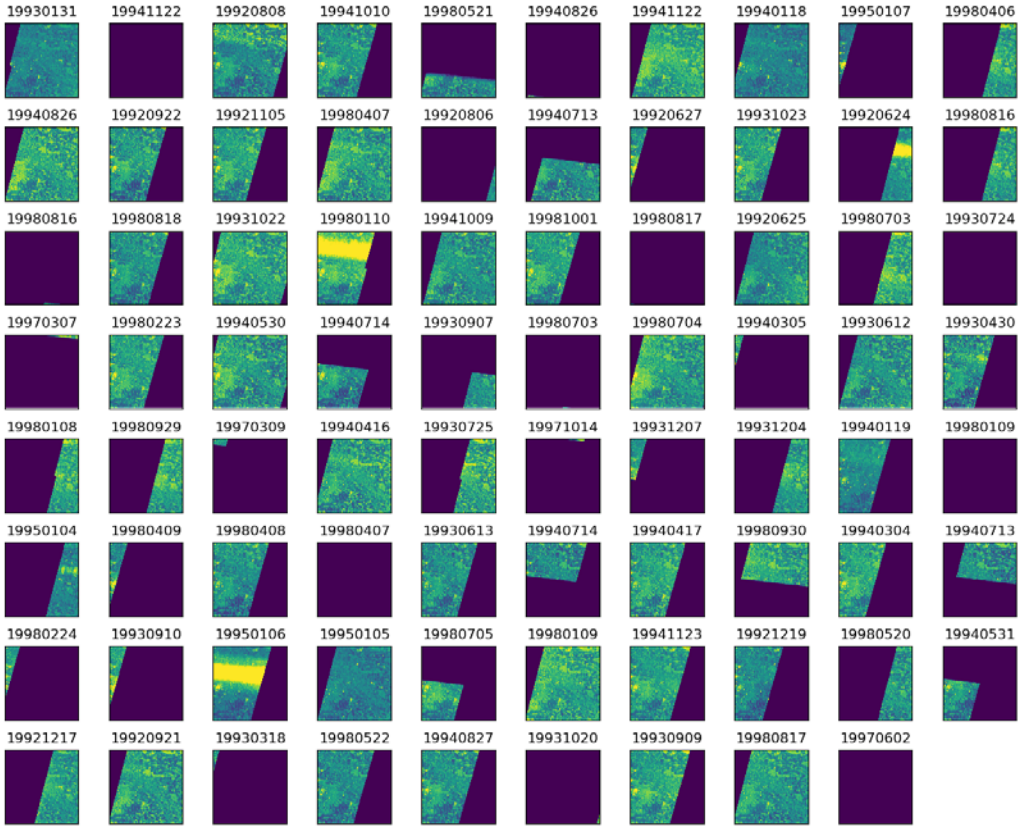

Figure 4.8: 1° x 1° tiles of L-HH backscatter acquired between 1992 and 1998 in an area between 10° and 11° East and 49° and 50° North. The scenes from 19920624, 19950106 and 19980110 show errors in the calibration.

Given the large number of ENVISAT ASAR observations available over Svalbard surge detection based on this sensor, at least over this region, is more straightforward than with JERS-1. An example of winter-to-winter ENVISAT ASAR radar backscatter changes for Nathorstbreen is displayed as normalised differences between maximum winter backscatter of subsequent years in *Figure 4.9*.

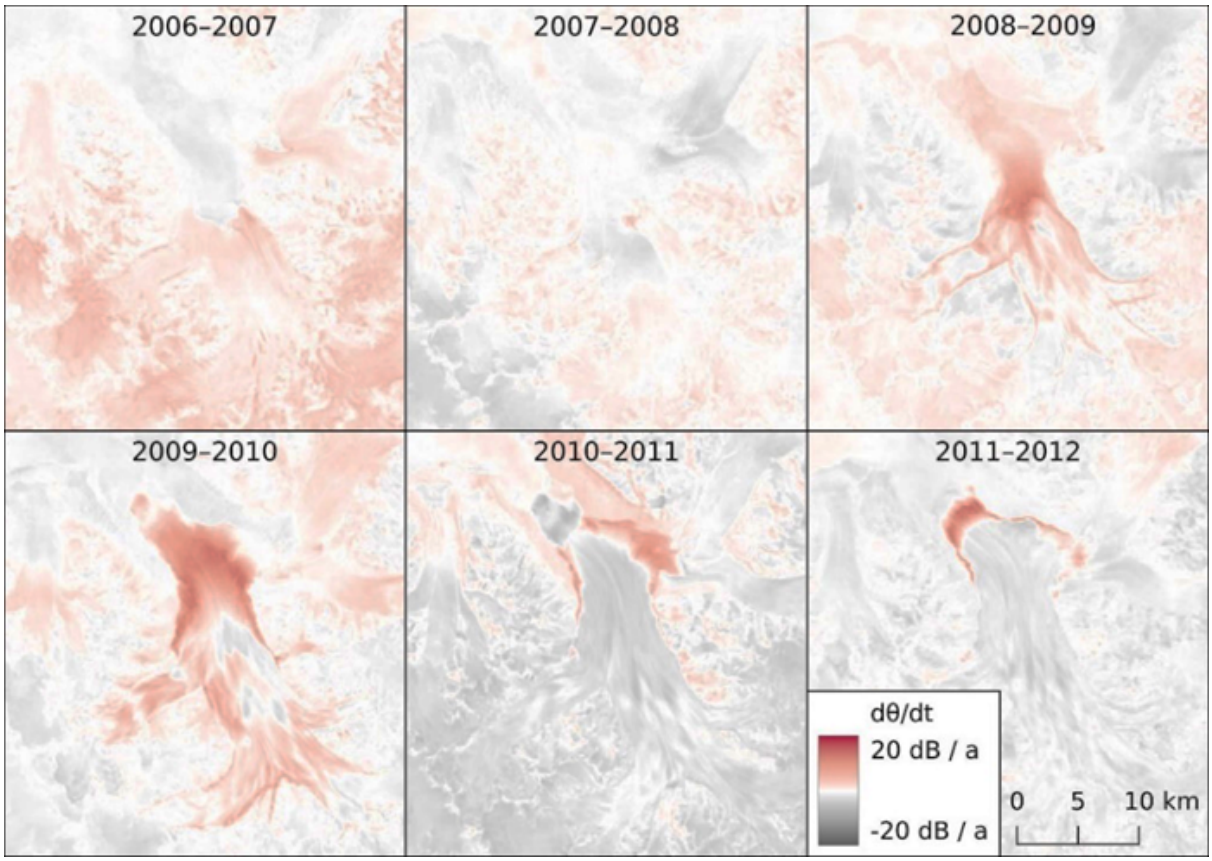

Figure 4.9: Example of winter-to-winter ENVISAT ASAR radar backscatter changes for Nathorstbreen, Svalbard, displayed as normalised differences between maximum winter backscatter of subsequent years. Red indicates increasing backscatter, grey decreasing backscatter over time. Increasing backscatter is interpreted as increasing crevassing and surge-type activity, and vice-versa.

4.3 Additional supporting data

4.3.1 Glacier flow velocities

Changes in ice velocity are a very suitable indicator to detect and characterise glacier surges. In support of the above method and processing line, velocity time series will be used to cross-check detections based on the primary method based on backscatter changes. Such velocity time series will be produced using standard Glacier_cci offset tracking methods applied to Sentinel-1 and Sentinel-2 data (see previous ATBDs, e.g. [RD2]). On a principle level, such velocity time series help to characterise the observed backscatter changes in terms of surge start, intensity, and end. On the level of individual glaciers such time series help to clarify interpretation uncertainties and to validate detections based on SAR backscatter (*Figure 4.2*, panels g-i).

4.3.2 Elevation change patterns

Elevation changes patterns over glaciers can indicate surge-type glaciers. Abnormal (compared to average glacier behaviour in a region) mass build-up in the accumulation area and pronounced thinning in the ablation area can point to a surge-type glacier in quiescent phase. Abnormal thickness loss in the accumulation area and thickness increase in the ablation area can point to a glacier during surge. Elevation change patterns can thus be used for an independent validation of surges as detected from radar backscatter, or to support related interpretations. To support the above methods and processing line, elevation differences are used, either processed using standard Glacier_cci elevation differences (reference to older ATBDs), or existing elevation changes, most prominently the global glacier elevation differences derived from ASTER (Hugonnet et al., 2021; based among others on Glacier_cci methodology (*Figure 4.10*)).

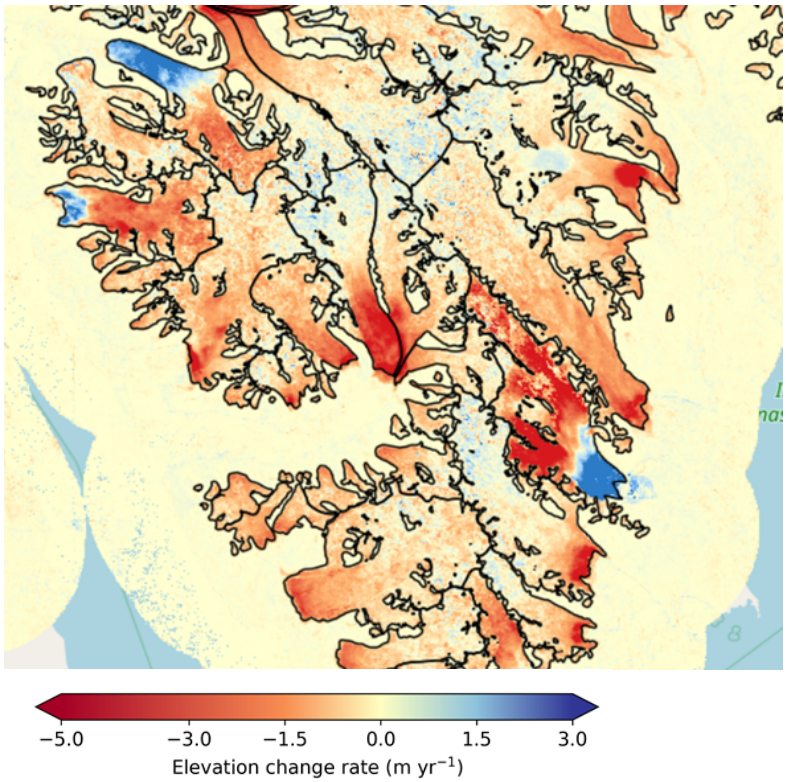

Figure 4.10: Elevation differences over glaciers in south-west Svalbard, 2010-2019 from Hugonnet et al. (2021). Dark blue zones over glacier tongues indicate pronounced thickening, indicative of glaciers in surge phase/advance.

4.3.3 Interpretation of optical images

Optical satellite images are a valuable tool to support glacier surge detection and are here used for clarification of uncertain backscatter-based detections. Visual surge indicators are among others enhanced crevassing, looped moraines, sheared-off tributary glaciers or abnormal glacier advances (Round and others, 2017, Muhammad and others, 2021, Truffer and others, 2021, Bevington & Copland, 2014, Steiner and others, 2018) (*Figure 4.11*). Such information is visually interpreted by an operator based on optical satellite data from around the date of surges as detected through backscatter surges.

Figure 4.11: Sentinel-2 image of surges at Chongtar Glacier, Karakoram, 4. Sept. 2022, showing glacier advances, crevassing, looped moraines etc. For details see Paul et al. (2022).

5. References

Bevington, A. and L Copland (2014). Characteristics of the last five surges of Lowell Glacier, Yukon, Canada, since 1948. Journal of Glaciology 60 (219), 113-123. doi.org/10.3189/2014JoG13J134

Copland, L., M.J. Sharp and J.A. Dowdeswell (2003). The distribution and flow characteristics of surge-type glaciers in the Canadian High Arctic. Annals of Glaciology, Vol 36 36, 73-81; doi.org/10.3189/172756403781816301

ESA EXPRO+ AlpGlacier consortium (2023). D3.1 - Algorithm Theoretical Basis Document Version 2. ESA EXPRO+ AlpGlacier project (Contract: 4000133436/20/I-NB). In review.

Foresta, L., N. Gourmelen, F. Pálsson, P. Nienow, H. Björnsson, and A. Shepherd (2016). Surface elevation change and mass balance of Icelandic ice caps derived from swath mode CryoSat-2 altimetry. Geophysical Research Letters, 43, 12,138–12,145; doi.org/10.1002/2016GL071485

Frey, O., Santoro, M., Werner, C.L. and Wegmuller, U. (2013). DEM-based SAR pixel-area estimation for enhanced geocoding refinement and radiometric normalization. IEEE Geosci. Remote Sens. Lett. 10, 48–52.

Grant, K.L., C.R. Stokes and I.S. Evans (2009). Identification and characteristics of surge-type glaciers on Novaya Zemlya, Russian Arctic. Journal of Glaciology 55(194), 960-972. doi.org/10.3189/002214309790794940

Gorelick, N., M. Hancher, M. Dixon, S. Ilyushchenko, D. Thau and R. Moore (2017). Google Earth Engine: Planetary-scale geospatial analysis for everyone. Remote Sensing of Environment, 202, 18-27; doi.org/10.1016/j.rse.2017.06.031

Helm, V., Humbert, A. and Miller, H. (2014). Elevation and elevation change of Greenland and Antarctica derived from CryoSat-2. The Cryosphere, 8(4), 1539–1559; doi.org/10.5194/tc-8-1539-2014

Hugonnet, R. and 10 others (2021). Accelerated global glacier mass loss in the early twenty-first century. Nature 592 (7856), 726-731; doi.org/10.1038/s41586-021-03436-z

Jakob, L. and Gourmelen, N. (2023). Glacier mass loss between 2010 and 2020 dominated by atmospheric forcing. Geophysical Research Letters, 50(8), e2023GL102954; doi.org/10.1029/2023GL102954

Kääb, A., Winsvold S.H., Altena B, Nuth C., Nagler T. and Wuite J. (2016). Glacier remote sensing using Sentinel-2. Part I: Radiometric and geometric performance, and application to ice velocity. Remote Sensing, 8(7), 598; doi.org/10.3390/rs8070598

Leclercq P.W., A. Kääb and B. Altena (2021). Brief communication: Detection of glacier surge activity using cloud computing of Sentinel-1 radar data. The Cryosphere 15(10), 4901-4907; doi.org/10.5194/tc-15-4901-2021

Maddalena, J.M. (2021). Elevation and Volumetric changes to the Greenland Ice Sheet derived from Sentinel-3 Satellite Radar Altimetry (unpublished doctoral dissertation). School of Geographical Sciences, University of Bristol.

Muhammad, S. and 8 others (2021). A holistic view of Shisper Glacier surge and outburst floods: from physical processes to downstream impacts. Geomatics Natural Hazards & Risk 12(1), 2755-2775; doi.org/10.1080/19475705.2021.1975833

Nagler, T., Rott, H., Ripper, E., Bippus, G. and Hetzenecker, M. (2016). Advancements for Snowmelt Monitoring by Means of Sentinel-1 SAR. Remote Sensing 8, 348; doi.org/10.3390/rs8040348

Paul, F. (2002): Changes in glacier area in Tyrol, Austria, between 1969 and 1992 derived from Landsat 5 TM and Austrian Glacier Inventory data. International Journal of Remote Sensing, 23 (4), 787-799.

Paul, F., S.H. Winsvold, A. Kääb, T. Nagler and G. Schwaizer (2016): Glacier Remote Sensing Using Sentinel-2. Part II: Mapping glacier extents and surface facies, and comparison to Landsat 8. Remote Sensing , 8(7), 575; doi.org/10.3390/rs8070575.

Paul, F., Piermattei, L., Treichler, D., Gilbert, L., Girod, L., Kääb, A., Libert, L., Nagler, T., Strozzi, T. and Wuite, J. (2022). Three different glacier surges at a spot: what satellites observe and what not. The Cryosphere, 16, 2505–2526; doi.org/10.5194/tc-16-2505-2022.

Paul, F., Baumann, S., Anderson, B. and Rastner, P. (2023): Deriving a year 2000 glacier inventory for New Zealand from the existing 2016 inventory. Annals of Glaciology, 90; doi.org/10.1017/aog.2023.20

Round, V., S. Leinss, M. Huss, C. Haemmig and I. Hajnsek (2017). Surge dynamics and lake outbursts of Kyagar Glacier, Karakoram. The Cryosphere 11(2), 723-739; doi.org/10.5194/tc-11-723-2017

Sakai, A. (2019): Brief communication: Updated GAMDAM glacier inventory over high-mountain Asia , The Cryosphere, 13, 2043–2049; doi.org/10.5194/tc-13-2043-2019

Sandmeier, S.R. and Itten, K.I. (1997). A physically-based model to correct atmospheric and illumination effects in optical satellite data of rugged terrain. IEEE Transactions on Geoscience and Remote Sensing 35, 708–717; doi.org/10.1109/36.581991

Santoro, M., Beer, C., Cartus, O., Schmullius, C., Shvidenko, A., McCallum, I., and Wiesmann, A. (2011). Retrieval of growing stock volume in boreal forest using hyper-temporal series of Envisat ASAR ScanSAR backscatter measurements. Remote Sensing of Environment, 115, 490–507.

Santoro, M., Wegmüller, U., Lamarche, C., Bontemps, S., Defourny, P. and Orino, O. (2015). Strengths and weaknesses of multi-year Envisat ASAR backscatter measurements to map permanent open water bodies at global scale, Remote Sensing of Environment, Volume 171, 2015, Pages 185-201, ISSN 0034-4257; doi.org/10.1016/j.rse.2015.10.031

Santoro, M., Cartus, O., Carvalhais, N., Rozendaal, D. M. A., Avitabile, V., Araza, A., de Bruin, S., Herold, M., Quegan, S., Rodríguez-Veiga, P., Balzter, H., Carreiras, J., Schepaschenko, D., Korets, M., Shimada, M., Itoh, T., Moreno Martínez, Á., Cavlovic, J., Cazzolla Gatti, R., da Conceição Bispo, P., Dewnath, N., Labrière, N., Liang, J., Lindsell, J., Mitchard, E. T. A., Morel, A., Pacheco Pascagaza, A. M., Ryan, C. M., Slik, F., Vaglio Laurin, G., Verbeeck, H., Wijaya, A., and Willcock, S. (2021). The global forest above-ground biomass pool for 2010 estimated from high-resolution satellite observations, Earth Syst. Sci. Data, 13, 3927–3950; doi.org/10.5194/essd-13-3927-2021

Smith, B., Jelley, B.P., Dickinson, S., Sutterley, T., Neumann, T. and Harbeck, K. (2022). Atlas/icesat-2 l3b gridded Antarctic and Greenland height change, version 2. NASA National Snow and Ice Data Center Distributed Active Archive Center. doi.org/10.5067/ATLAS/ATL15.002

Shepherd, A., Gilbert, L., Muir, A. S., Konrad, H., McMillan, M., Slater, T., Briggs, K. H., Sundal, A. V., Hogg, A. E. and Engdahl, M. E. (2019). Trends in Antarctic ice sheet elevation and mass. Geophysical Research Letters, 46(14), 8174–8183; doi.org/10.1029/2019GL082182

Shimada, M. and Isogouchi, O. (2002). JERS-1 SAR mosaics of Southeast Asia using calibrated path images. Int. J. Remote Sensing, 23 (7), 1507–1526.

Shimada, M. and Ohtaki, T. (2010). Generating large-scale high-quality SAR mosaic datasets: Application to PALSAR data for global monitoring. IEEE Journal of Selected Topics in Applied Earth Observations and Remote Sensing, 3 (4), 637-656.

Shimada, M., Itoh, T., Motooka, T., Watanabe, M., Shiraishi, T., Thapa, R. and Lucas, R. (2014). New global forest/non-forest maps from ALOS PALSAR data (2007–2010). Remote Sensing of Environment, 155, 13-31.

Steiner, J.F., P.D.A. Kraaijenbrink, S.G. Jiduc and W.W. Immerzeel (2018). Brief communication: The Khurdopin glacier surge revisited - extreme flow velocities and formation of a dammed lake in 2017. The Cryosphere 12(1), 95-101; doi.org/10.5194/tc-12-95-2018.

Tepes, P., Gourmelen, N., Nienow, P., Tsamados, M., Shepherd, A. and Weissgerber, F. (2021). Changes in elevation and mass of Arctic glaciers and ice caps, 2010–2017. Remote Sensing of Environment, *261*, 112481. doi.org/10.1016/j.rse.2021.112481

Truffer, M. and 10 others (2021). Chapter 13 - Glacier surges. In Haeberli W and C Whiteman, eds. Snow and Ice-Related Hazards, Risks, and Disasters (2nd Edition), Elsevier, 417-466.

Vermote, E., Tanré, D., Deuzé, J.L., Herman, M., Morcrette, J.J. and Kotchenova, S.Y. (2006). Second Simulation of the Satellite Signal in the Solar Spectrum – Vector (6SV) User Guide Version 3. https://ltdri.org/6spage.html

Vermote, E.F., Tanré, D., Deuzé, J.L., Herman, M. and Morcrette, J.J. (1997). Second simulation of the satellite signal in the solar spectrum, 6s: an overview. IEEE Transactions on Geoscience and Remote Sensing 35, 675–686; doi.org/10.1109/36.581987

6. Acronyms

ALOS	Advanced Land Observing Satellite
ASTER	Advanced Spaceborne Thermal Emission and Reflection Radiometer
ATBD	Algorithm Theoretical Baseline Document
db	Decibel
DN	Digital Number
DEM	Digital Elevation Model
ERS	European Remote Sensing Satellite
ENVISAT	Environmental Satellite
ESA	European Space Agency
ETM+	Enhanced Thematic Mapper plus
GCP	Ground Control Point
GDEM	Global DEM
GEE	Google Earth Engine
GLF	Glacier Facies
GRD	Ground Range Detected
ICESat	Ice, Cloud, and land Elevation Satellite
InSAR	Interferometric SAR
IV	Ice Velocity
JERS	Japanese Earth Resource Satellite
LOS	Line Of Sight
LUT	Look Up Table
MEaSUREs	Making Earth System Data Records for Use in Research Environments
MSS	Multi-Spectral Scanner
NDI	Normalized Difference Image
OLI	Operational Land Imager
PALSAR	Phased Array type L-band Synthetic Aperture Radar
POCA	Point of closest approach
RADAR	Radio Detection and Ranging
RD	Reference Document
RGI	Randolph Glacier Inventory
RMS	Root Mean Square
SAR	Synthetic Aperture Radar
SAOCOM	SAtélite Argentino de Observación COn Microondas
SLC	Single Look Complex
SRTM	Shuttle Radar Topography Mission
SWIR	Shortwave Infrared
TM	Thematic Mapper
UTM	Universal Transverse Mercator
WGS	World Geodetic System